GEORG-AUGUST-UNIVERSITÄT
GÖTTINGEN

Fakultät für
Physik

Bachelor's Thesis

Untersuchung der W→ qq′ Jetrekonstruktion bei Jets mit großem Radius in hh→WW$\gamma\gamma$ Zerfällen mit dem ATLAS Detektor

Investigation of W→ qq′ Reconstruction using large-R jets in hh→WW$\gamma\gamma$ events with the ATLAS detector

prepared by

Kieran Amos

from Stemwede

at the II. Physikalischen Institut

Thesis number:	II.Physik-UniGö-BSc-2016/06
Thesis period:	4th April 2016 until 11th July 2016
First referee:	Prof. Dr. Stan Lai
Second referee:	Prof. Dr. Ariane Frey

Abstract

In dieser Arbeit wird die optimale Rekonstruktion eines hadronisch zerfallenden, *boosted, on-shell* W Bosons im Zerfallskanal $hh \to WW\gamma\gamma$ am ATLAS Detektor mit simulierten Ereignissen bei einer Schwerpunktsenergie von $\sqrt{s} = 13\,\text{TeV}$ untersucht. Hierzu wird evaluiert, inwiefern eine Auswahl an Jetkollektionen und Strukturvariablen den obigen Prozess von einem *single Higgs* $h \to \gamma\gamma$ Zerfall unterscheiden können. Die Analyse wird für zwei verschiedene Jet-p_T Bereiche wiederholt und es stellt sich heraus, dass die besten Ergebnisse im hohen p_T Bereich mit dem Energiekorrelationsverhältnis C_2 erzielt werden können. Erreicht wird eine *background exclusion rate* von $94.4 \pm 1.3\%$ bei einer *signal efficiency* von 50%.

Abstract

This thesis deals with the optimal reconstruction of the hadronically decaying, boosted, on-shell W boson from the di-Higgs decay channel $hh \to WW\gamma\gamma$ using simulated events with the ATLAS detector at a centre of mass energy of $\sqrt{s} = 13\,\text{TeV}$. To achieve this, a combination of jet collections and substructure variables are evaluated for their ability to discriminate the process from a background of single Higgs $h \to \gamma\gamma$ decays. The analysis is repeated for two different jet-p_T regions. It is shown that the best results can be achieved in the high-p_T range with the Energy Correlation Function ratio C_2 and that this achieves a background exclusion rate of $94.4 \pm 1.3\%$ at 50% signal efficiency.

Contents

Nomenclature

Variables

Variable	Meaning	Dimension
E	Energy	GeV
p_{T}	Transverse Momentum	GeV
m	Mass	GeV
θ	Polar Angle	°; –
ϕ	Azimuth Angle	°; –
y	Rapidity	–
η	Pseudorapidity	–
ΔR	Angular Distance in ϕ-η Space	–
ϵ	Efficiency	–
C_2, D_2	Energy Correlation Function Ratios	–
τ_{21}, τ_{21}^{wta}	N-Subjettiness Variables	–

Abbreviations

Acronym	Meaning
BSM	Beyond Standard Model
C/A	Cambridge/Aachen
CERN	European Organization for Nuclear Research
ECF	Energy Correlation Function
GGF	Gluon-Gluon Fusion
LHC	Large Hadron Collider
max	Maximum
MC	Monte-Carlo
min	Minimum

Acronym	**Meaning**
QCD	Quantum Chromodynamics
SM	Standard Model
VBF	Vector Boson Fusion
h	Standard Model Higgs Boson
H	Beyond Standard Model Heavy Higgs Boson
W	Charged Electro-Weak Gauge Boson
j	Jet
q, $\bar{q}$	Quark, Anti-Quark
g	Gluon
γ	Photon

1. Introduction

Since the discovery of the Higgs boson at the ATLAS and CMS experiments in 2012 [1, 2], the focus of research has been on confirming its properties as predicted by the Standard Model (SM) of particle physics. One particular property that has not yet been measured is the self-coupling of the Higgs boson which is at least, in principle, detectable via the simultaneous production of two Higgs bosons in hadron colliders. This process also opens up a possible window into Beyond Standard Model (BSM) physics where a heavier version of the Higgs boson could create a resonance of the SM Higgs pairs in $H \to hh$ decays [3]. In either case the process would be characterised by the decay of the hh pair. There are many final states that could conceivably be extracted from the background such as $hh \to b\bar{b}b\bar{b}$ [4] or $hh \to b\bar{b}\gamma\gamma$ [5]. The process of interest in this analysis is $hh \to WW^*\gamma\gamma$ [6] based on the ATLAS detector at a centre of mass energy of $\sqrt{s} = 13\,\text{TeV}$. Candidate events can be identified by the presence of the two photons in the electromagnetic calorimeter. Depending on the centre of mass energy of the colliding partons in the non-resonant case and the mass of the heavy higgs boson in the resonant case, the decay products of one or even both of the highly boosted W bosons can be contained within a hadronic jet with a large radius. The aim of this thesis is to identify the optimal method of reconstructing the on-shell W as a distinct jet, assuming it has decayed hadronically.

The thesis proceeds as follows: Section 2 gives a brief summary of the Standard Model of particle physics, an overview of the Higgs mechanism and the relevant characteristics of the Higgs boson, and finally a discussion on the nature of parton showering and hadronisation. Section 3 introduces the ATLAS detector at the Large Hadron Collider (LHC) at CERN as the experimental setup for this analysis. Section 4 details the Monte-Carlo generated signal and background samples used for the analysis and presents the jet algorithms and jet substructure variables as the tools used. Finally, Section 5 is dedicated to the presentation of the results.

2. Theory

2.1. The Standard Model of Particle Physics

The Standard Model attempts to explain the world in terms of fundamental particles and forces. Developed over the course of the last half-century, it currently provides the best known theoretical description of the building blocks of our universe and many of its predictions have been verified in countless experiments.

According to the Standard Model, matter is made up of 12 spin-$\frac{1}{2}$ particles known as fermions, as depicted in Figure 2.1. In the first few decades of the 20^{th} century, it was discovered that bulk matter is made up of atoms, consisting of protons (p) and neutrons (n) in the atomic core and surrounded by lighter electrons (e^-). A great breakthrough came with the discovery that the proton and neutron are not fundamental particles, but are comprised of *up*-quarks (u) and *down*-quarks (d). Along with the electron and the electron neutrino (ν_e), whose discovery was needed to account for missing momentum in beta decays, these quarks make up the first generation of fermions. As experiments began probing ever higher energies the existence of a second and third generation was uncovered with heavier fermions that are otherwise identical to those of the first generation. For the quarks the additions are (c), (s), (t) and (b) denoting the *charm*-quark, *strange*-quark, *top*-quark and *bottom*-quark respectively. The remaining particles are referred to as leptons. The first generation electron (e^-) is complemented by the muon (μ^-) and the tau lepton (τ^-) along with their associated neutrinos (ν_e), (ν_μ), (ν_τ). Generally, later generation fermions quickly decay into first generation members, which explains the observation that everything in nature is built out of the lighter fermions. Finally, each fermion has an associated anti-particle that is identical in mass and lifetime but has opposite charges and other fundamental properties. For example the electron is paired with the positron (e^+), and each neutrino (ν) and quark (q) is mirrored by an anti-neutrino ($\bar{\nu}$) and an anti-quark ($\bar{q}$).

Along with their associated mass, charge and spin, all particles can be classified by the forces they experience. The four known fundamental forces are given in Table 2.1. Note that gravity is not included in the Standard Model, and can be neglected in High Energy

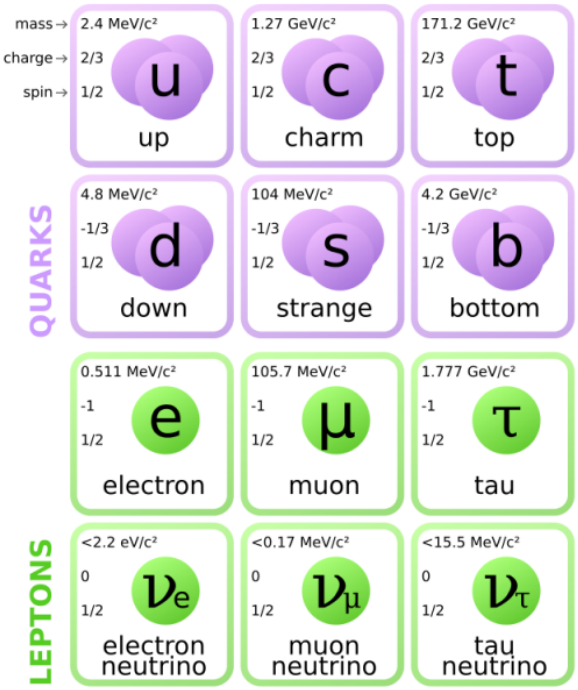

Figure 2.1.: The twelve fundamental fermions of the Standard Model along with their basic properties.

Force	Relative Stength	Boson		Mass [GeV]
Strong	1	Gluon	(g)	0
Electromagnetism	10^{-3}	Photon	(γ)	0
Weak	10^{-8}	W Boson	($W^{\pm}$)	80.4
		Z Boson	(Z)	91.2
Gravity	10^{-37}	Graviton?	(G)	0

Table 2.1.: The four fundamental forces and their associated bosons.

Physics experiments as it is over 30 orders of magnitude weaker than the other forces. Each force is mediated through the exchange of particles with integer spins called bosons and can be described using a local gauge symmetry. The simplest example is the electromagnetic force with symmetry U(1) resulting in the strength of the photon's coupling being proportional to a single parameter, the electric charge Q. The theory of the electromagnetic interaction is known as Quantum Electrodynamics (QED). The other two forces are the strong nuclear force and the weak nuclear force.

2.1.1. The Strong Nuclear Force

The theory of the strong nuclear force is called Quantum Chromodynamics or QCD. Due to its strength, this force will tend to dominate particle interactions whenever possible. To take part in an interaction using the strong force a particle must carry an appropriate charge known as colour charge, where the three different "colours", labelled r, g and b, are the orthogonal states of the corresponding SU(3) symmetry. The leptons do not carry a colour charge and consequently quarks are the only fermions that are involved in strong interactions.

An important experimental observation in QCD is that neither quarks nor gluons have ever been seen individually. This is explained by the hypothesis of *colour confinement* which arises from gluon self interactions and states that only bound colourless states of quarks can ever be observed as free particles. The permissible states are referred to as mesons $|q\bar{q}\rangle$, baryons $|qqq\rangle$ and antibaryons $|\bar{q}\bar{q}\bar{q}\rangle$.

In Quantum Field Theory a process between initial and final particle states can be examined using the sum of all possible Feynman diagrams that correspond to these states. Although there are infinitely many diagrams for each possible process, their individual contribution is proportional to the number of vertices with each vertex providing a factor $\alpha_S(q^2)$ known as the coupling constant which is dependent on the square of the momentum transferred via the interaction q^2 and is specific to the force involved. The coupling constant for the strong force α_S decreases strongly with q^2. This is known as *asymptotic freedom* and as a result, for low energies α_S approaches unity making a perturbative approach for bound hadrons and low-energy jets impossible.

2.1.2. The Weak Nuclear Force

The weak interaction differs from the other two forces of the Standard Model in a number of ways. The W^+, W^- and Z bosons that mediate it are massive particles with their own decay modes and are capable of coupling to all fundamental fermions. Additionally, only the weak force is found to violate charge parity (CP) [7]. As a consequence of parity violation, charged-current W bosons only couple to left chiral particle states and right chiral anti-particle states.

Despite its small strength compared to the strong and electromagnetic forces, this mechanism plays an important role in many decays as it is the only one capable of changing particle flavour via an interaction vertex involving the W boson. The charged leptons are always paired with their corresponding neutrinos of their flavour. For the quarks, the exchanged particles must differ by one unit of electric charge with the precise strength of

each individual coupling given by the Cabibbo-Kobayashi-Maskawa (CKM) matrix:

$$\begin{pmatrix} \mathrm{d}' \\ \mathrm{s}' \\ \mathrm{b}' \end{pmatrix} = \begin{pmatrix} \mathrm{V_{ud}} & \mathrm{V_{us}} & \mathrm{V_{ub}} \\ \mathrm{V_{cd}} & \mathrm{V_{cs}} & \mathrm{V_{cb}} \\ \mathrm{V_{td}} & \mathrm{V_{ts}} & \mathrm{V_{tb}} \end{pmatrix} \begin{pmatrix} \mathrm{d} \\ \mathrm{s} \\ \mathrm{b} \end{pmatrix}.$$

Here the weak eigenstates d′, s′ and b′ are expressed as linear combinations of the observed mass states d, s and b. The square of the absolute value of each element is then proportional to the strength of each coupling between the W and the two quarks. Because the off-diagonal elements are non-zero, generation mixing is allowed for quarks. In experiments, the diagonal elements describing reactions within the same generation are found to dominate.

One of the ultimate goals of particle physics is to incorporate the individual theories for the forces into a single unifying theory. This has been achieved for the weak and electromagnetic forces in the Glashow-Salam-Weinberg (GSM) Model [8–10]. The $\mathrm{SU}(2)_L$ symmetry from the weak interaction is extended with a modified version of electromagnetic symmetry to make $\mathrm{SU}(2)_L \times \mathrm{U}(1)_Y$. The electric charge Q and the third component of weak isospin $I_W^{(3)}$ make up the electroweak charge known as hypercharge $Y = 2(Q - I_W^{(3)})$.

2.2. The Higgs Mechanism

The Standard Model Lagrangian is required to be invariant under local gauge transformations. This is easily achieved for the massless photon and gluon, but the introduction of mass-terms into the Lagrangians for the massive weak bosons as well as the fermions breaks the gauge symmetry. The situation can be remedied in a process known as *spontaneous symmetry breaking*, where a field is introduced that consists of a weak isospin doublet of two complex scalar fields:

$$\phi = \begin{pmatrix} \phi^+ \\ \phi^0 \end{pmatrix} = \frac{1}{\sqrt{2}} \begin{pmatrix} \phi_1 + i\phi_2 \\ \phi_3 + i\phi_4 \end{pmatrix}.$$

The resulting Lagrangian includes terms describing the Higgs potential:

$$V(\phi) = \mu^2 \phi^\dagger \phi + \lambda (\phi^\dagger \phi)^2.$$

For $V(\phi)$ to have a minimum that corresponds to the vacuum state, it is necessary that $\lambda > 0$. The form of the potential for a single complex scalar field is shown in Figure 2.2 for $\mu^2 < 0$.

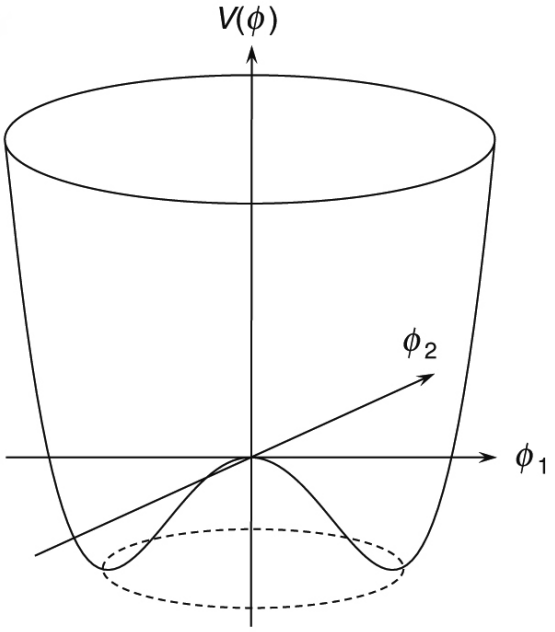

Figure 2.2.: The Higgs potential $V(\phi)$ for a complex, scalar field with $\lambda > 0$ and $\mu^2 < 0$.

In this case the minimum is given as

$$\phi^\dagger \phi = \frac{v^2}{2} = -\frac{\mu^2}{2\lambda}.$$

Writing the Higgs Doublet in the unitary gauge and accommodating the massless photon leads to

$$\phi(x) = \frac{1}{\sqrt{2}} \begin{pmatrix} 0 \\ v + h(x) \end{pmatrix}$$

with h(x) as the physical Higgs field.
The mass terms of the gauge bosons can be determined from the Lagrangian $(D_\mu \phi)^\dagger (D^\mu \phi)$, where the ordinary derivatives have been replaced by the covariant derivatives of the $\mathrm{SU}(2)_L \times \mathrm{U}(1)_Y$ local gauge symmetry

$$\partial_\mu \rightarrow D_\mu = \partial_\mu + i g_W \mathbf{T} \cdot \mathbf{W}_\mu + i g' \frac{Y}{2} B_\mu$$

g_W and g' are the coupling constants of the $\mathrm{SU}(2)_L \times \mathrm{U}(1)_Y$ local gauge symmetry, $\mathbf{T}$ contains the generators of SU(2), Y is the hypercharge and W_μ and B_μ are the gauge boson fields. The four original degrees of freedom now correspond to the three gauge bosons of the electroweak theory as well as an additional scalar, spin-0 particle from the

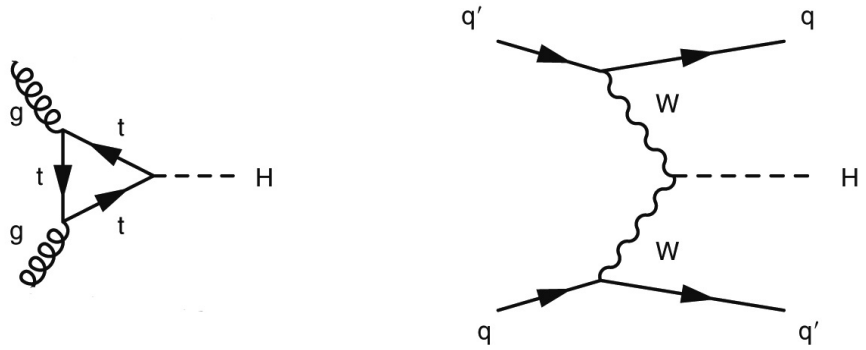

Figure 2.3.: The two most common Feynman diagrams for the production of the Higgs boson.

excitation of the Higgs field:

$$m_W = \frac{1}{2} g_W v, \quad m_Z = \frac{1}{2} v \sqrt{g_W^2 + g'^2}, \quad m_A = 0, \quad m_h = \sqrt{2\lambda} v.$$

One of the main goals of LHC at CERN was the detection of the Higgs boson, and in July 2012 the two main experiments, ATLAS and CMS, independently announced the detection of a particle with a mass of 125 GeV that was subsequently shown to be the Higgs boson [1, 2]. The current best value for the mass of the Higgs boson is $m_h = 125.09 \pm 0.21(\text{stat.}) \pm 0.11(\text{syst.})\,\text{GeV}$ [11].

2.2.1. Higgs Production and Decay Modes

The detection of Higgs bosons is complicated both by the high energy required and the low cross section compared to the background events. The LHC was specifically designed with this in mind and operates at a high centre of mass energy at the luminosity frontier. The two most common Feynman diagrams for the production of a Higgs boson are shown in Figure 2.3. In the first case, known as *gluon-gluon fusion* (GGF), two gluons from the collection of virtual quarks and gluons within the colliding hadrons create a Higgs boson via a virtual top loop. In the second case, *vector boson fusion* (VBF), the Higgs boson is created directly from the annihilation of two W or Z bosons that are radiated by initial quarks in interacting protons. While the GGF cross section is much larger, the identification of the Higgs boson signal in this production mode is complicated by the large QCD background. For the VBF process the scattered quarks from the colliding hadrons are expected to propagate in the beam direction, and the decay products of the Higgs boson can be more easily separated from the relevant backgrounds. The cross sections for both processes at $\sqrt{s} = 13\,\text{TeV}$ and $m_h = 125\,\text{GeV}$ are shown in Table 2.2. Included are the cross sections for Higgs Radiation (Wh, Zh) and tth and bbh channels where a Higgs

Process	Cross section [pb]
GGF	43.92
VBF	3.748
WH	1.380
ZH	0.9753
ttH	0.5085
bbH	0.5116

Table 2.2.: Cross sections for Higgs boson production at $\sqrt{s} = 13\,\text{TeV}$ and $m_H = 125\,\text{GeV}$ [12]

Decay mode	Branching ratio
$h \to b\bar{b}$	57.8%
$h \to WW^*$	21.6%
$h \to gg$	8.6%
$h \to \tau^+\tau^-$	6.4%
$h \to c\bar{c}$	2.9%
$h \to ZZ^*$	2.7%
$h \to \gamma\gamma$	0.2%

Table 2.3.: The predicted branching ratios for a Higgs boson with mass $m_H = 125\,\text{GeV}$ [12].

boson is created in association with a top or bottom quark pair.

The Higgs boson can potentially decay in to all particles that have mass with the exception of the heavier top quark, but the coupling strength is proportional to the mass of the involved particles. The observed branching ratios for the observed 125 GeV Higgs boson are shown in Table 2.3. The difficulty of resolving decays involving jets make the $H \to \mathrm{q\bar{q}}$ modes unlikely candidates for the Higgs discovery with the possible exception of $H \to \mathrm{b\bar{b}}$ where the mesons containing b-quarks can be identified by the secondary vertices created at the point of their decay. In the case of the $\mathrm{W^+W^-}$ or $\tau^+\tau^-$ modes decaying leptonically, the undetectable neutrinos hamper the energy resolution. As a result, the Higgs Boson was observed using the much rarer top-loop induced $H \to \gamma\gamma$ channel and the $H \to ZZ^*$ channel where the Z bosons decay into four charged leptons.

So far only single Higgs production has been observed. This is consistent with the low cross section for pair produced Higgs bosons predicted by the Standard Model, but Beyond Standard Model (BSM) theories offer the possibility of observing significantly more di-Higgs events at current energies. Figure 2.4 shows leading order Feynman diagrams for non-resonant $gg \to hh$ production channels. A distinction can be made between models involving non-resonant pair production of the observed 125 GeV Higgs boson h in $gg \to hh$

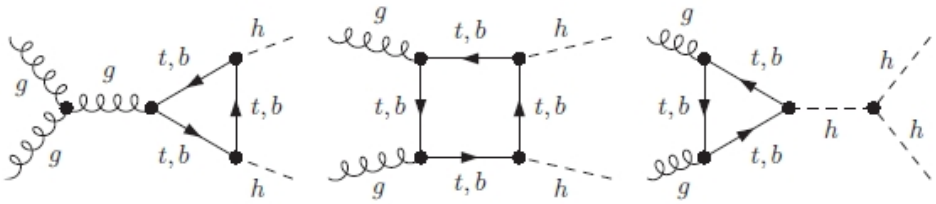

Figure 2.4.: Leading order Feynman diagrams for Standard Model $gg \to hh$ processes.

processes, such as light coloured scalars [13] or direct quartic vertices [14], and those where the Higgs boson pair are the product of a resonance from a heavier Higgs boson H in $gg \to H \to hh$, for example the two-Higgs-doublet model (2HDM) [3]. The non-resonant $gg \to hh$ cross section at $\sqrt{s} = 13\,\text{TeV}$ has been predicted to be 33.70 fb based on NNLO calculations [15]. The observed signal strengths of the various final decay products for the resonant case is strongly dependent on the mass of the heavy Higgs boson, which could range from $m_H = 2m_h$ into the TeV range. Estimations for the cross section at $\sqrt{s} = 13\,\text{TeV}$ include a multiplication of the SM cross section procuction rate by 18 for $m_H = 270\,\text{GeV}$ and 13 for $m_H = 420\,\text{GeV}$ [16].

2.3. Hadronisation and Parton Showers

In particle interactions, the relative strength of the strong force leads to cross sections involving quarks and gluons to dominate in reactions whenever possible, and a $\text{q}\bar{\text{q}}$ pair is often created travelling in opposite directions. As a result of colour confinement, the field energy between the increasingly isolated quarks grows until it is more energetically favourable for a new $\text{q}\bar{\text{q}}$ pair to be produced. This continuous process is known as a *parton shower* and results in sprays of coloured particles. The resulting particles propagate at high energies through the detector and as the partons are separated from their colour singlet state, additional ones are created in a cascade of QCD products until the initial energy is too spread out for further creation. Colour confinement ensures that individual partons are never observed but instead combine to form color singlet hadrons. This process is known as *hadronisation*. The resulting energy deposits in the calorimeters allow the definition of experimental observables based on calorimeter information. These are some of the most studied objects in experimental particle physics with a strong focus on understanding the nature of the strong interaction and on classifying the parton showers by the particle that seeded them. An example is determining the differences between a quark and a gluon initiated shower [17, 18].

Many models have been developed to understand the process of hadronisation. In general Matrix-element calculations to leading order (LO) are only effective for hard partons that can be easily identified. As the initial parton fragments, the number of calculations needed increases with the number of particles and the average energy of each element within the shower decreases leading to an increase of the strong coupling constant via asymptotic freedom and the system becoming evermore non-perturbative.
For soft radiation, additional approximations are used to generate the high numbers of particles needed to model the physical showers. Methods involve the calculation of average radiation lengths for which the parton does not radiate additional particles which is then iteratively applied to the daughter partons [19].
The result of hadronisation and parton showers are energy deposits spread across the calorimeters of particle detectors. Since there is no definitive way of clustering these deposits together based on the initial parton, many different methods have been developed. The resulting clusters are known as jets. Various jet reconstruction algorithms will be discussed in Section 4.2.

3. The Experimental Setup

3.1. The Large Hadron Collider

In collider experiments particles are smashed together in intersecting beams, and their energy is used to create heavy particles. These can subsequently decay into lighter, stable particles. Each interaction is governed by the strength of the relevant force, and analysing the resultant final state in specialized detectors allows insights into their precise nature.
The Large Hadron Collider (LHC) at CERN is currently the most powerful high-energy collider ever built. After approval for the project was granted in 1994, construction began in the 26.7 km tunnel previously used by the former LEP Collider, greatly reducing the total cost of the project. The LHC also makes use of the injection chain originally used by the previous experiment where particles are first accelerated in as series of smaller accelerators before injection into the main beam. At completion in 2008 the LHC operated at a center-of-mass energy of $\sqrt{s} = 7\,\text{TeV}$ with an increase to $\sqrt{s} = 8\,\text{TeV}$ in 2012. As of May 2015, after a two year pause for upgrades it is running at $\sqrt{s} = 13\,\text{TeV}$, and its final design energy envisioned for 2017-18 is $\sqrt{s} = 14\,\text{TeV}$. The design luminosity of the beams is $10^{34}\,\text{cm}^{-2}\,\text{s}^{-1}$ [20].
In its primary mode of operation, proton beams are inserted using a series of smaller synchrotrons and are then accelerated in opposite directions around two overlapping rings. Both rings can be divided into eight straight sections and eight curved sections. Major limiting factors on the maximum obtainable energy are the 1232 dipole magnets with a field strength of up to 8.33 T, cooled to 1.9 K and situated at the curved regions. At the maximum operating capacity the beams themselves consist of 2808 bunches, each containing approximately $1.15 \cdot 10^{11}$ protons. The collisions occur at four points of the rings on the straight segments at intervals of roughly 25 ns. Here the four main detectors are located. ATLAS and CMS are general-purpose detectors known for their discovery of the Higgs boson in 2012. They are complemented by the ALICE and LHCb detectors, which specialize in heavy-ion collisions and b-hadron CP violation, respectively.

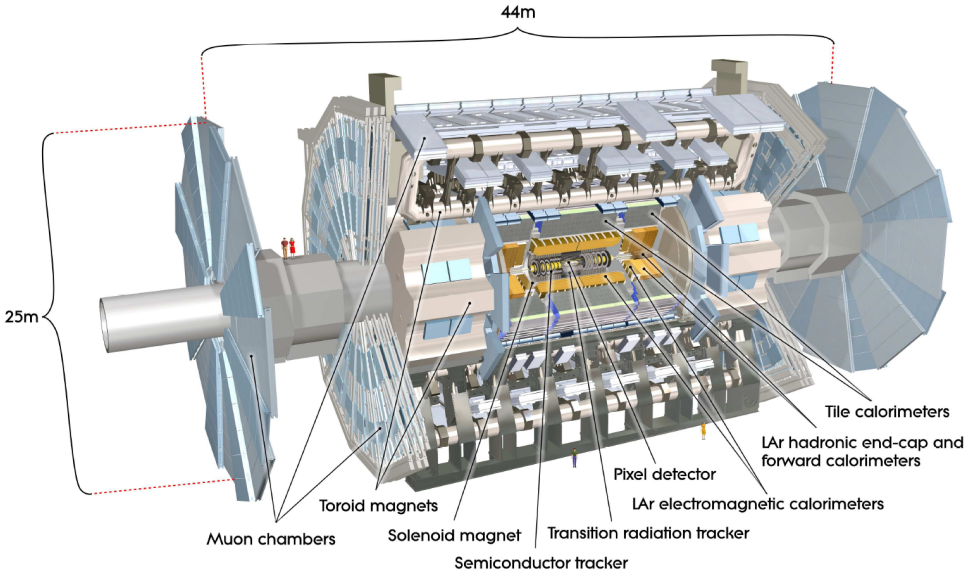

Figure 3.1.: An overview of the ATLAS detector.

3.2. The ATLAS Detector

3.2.1. Construction and Coordinates

The general-purpose ATLAS (A Toroidal LHC ApparatuS) detector is comprised of cylindrical layers and end-caps of various detector types constructed around a point where the beams intersect as shown in Figure 3.1. Particular requirements during its design were the precise measurement of muons in the outer muon spectrometers and full reconstruction capabilities in the calorimeters resulting in additional detector layers in the end-caps to account for events with low transverse momentum [21]. The trajectories of particles are described using cylindrical coordinates with the z-axis directed along the path of the colliding beams. The five main parameters used by ATLAS to classify the particle trajectories in the approximation of a homogeneous field are:

1. $\frac{1}{p_T}$ with transverse momentum $p_T = \sqrt{p_x^2 + p_y^2}$.
2. The azimuthal angle, ϕ.
3. $\mathrm{Cot}\,\theta$, where θ is the polar angle.
4. The impact parameter in the transverse direction with respect to the primary interaction vertex, d_0.
5. The impact parameter in the longitudinal direction with respect to the primary interaction vertex, z_0.

In addition, the rapidity of a particle defined as

$$y = \frac{1}{2} \ln \frac{E + p_z}{E - p_z}$$

where E is the energy of the particle and p_z its momentum in the direction of the beam is a useful concept as differences, Δy, are Lorentz invariant under boosts along the beam axis. The rapidity can be approximated by the pseudorapidity

$$\eta = \frac{1}{2} \ln \left(\frac{|\vec{p}| + p_z}{|\vec{p}| - p_z} \right) = - \ln \left[\tan \left(\frac{\theta}{2} \right) \right]$$

for highly relativistic particles. Differences in η are Lorentz invariant for massless particles and have the advantage of being dependent only on the detector coordinates and not on the particle properties.
The angular separation of particles in the detector can be measured using

$$\Delta R_{ij} = \sqrt{(\phi_i - \phi_j)^2 + (\eta_i - \eta_j)^2}.$$

The Inner Detector is 7 m long with a radius of 1.15 m and surrounded by a 2 T solenoid magnet. Building outwards from the central beam are a combination of pixel detectors, semiconductor strips and straw-tube detectors for transition radiation tracking. Divided into barrel and end-cap elements they provide full coverage for $|\eta| \leq 2.5$ with a resolution capability up to 12 µm in the radial direction. The purpose of the Inner Detector is to accurately measure charged particle tracks.
Outside of the solenoid the calorimeters measure the energy deposited in the dense outer materials. Granular liquid Argon is used for the electromagnetic sampling calorimeter and scintillator tiles for the hadronic calorimeter. Their combined coverage extends to $|\eta| = 4.9$, and together they extend over 13 m in the z direction and to a radius of 4.25 m. The muon spectrometer makes up the rest of the 46 m long, 25 m wide 7000 ton detector. The magnetic field required is created by toroidal magnets and a combination of trigger, and high-precision, gaseous tracking chambers provide almost full coverage.
An overview of the resolutions and angle coverages of the various detector components can be found in Table 3.1.

Detector component	**Required resolution**	**η coverage**	
		Measurement	Trigger
Tracking	$\sigma_{p_T}/p_T = 0.05\% \, p_T \oplus 1\%$	$\lvert\eta\rvert \pm 2.5$	
EM calorimeter	$\sigma_E/E = 10\%/\sqrt{E} \oplus 0.7\%$	$\lvert\eta\rvert \pm 3.2$	$\lvert\eta\rvert \pm 2.5$
Hadronic calorimetry (jets)			
barrel and end-cap	$\sigma_E/E = 50\%/\sqrt{E} \oplus 3\%$	$\lvert\eta\rvert \pm 3.2$	$\lvert\eta\rvert \pm 3.2$
forward	$\sigma_E/E = 100\%/\sqrt{E} \oplus 10\%$	$3.1 < \lvert\eta\rvert < 4.9$	$3.1 < \lvert\eta\rvert < 4.9$
Muon spectrometer	$\sigma_{p_T}/p_T = 10\%$ at $p_T = 1\,\text{TeV}$	$\lvert\eta\rvert \pm 2.7$	$\lvert\eta\rvert \pm 2.4$

Table 3.1.: General performance of the ATLAS detector showing the resolutions and coverage angles of the various components. E and p_T are in GeV [22].

3.2.2. Trigger System

At peak luminosity, the event rate within the ATLAS detector is $\sim 10^9\,\text{Hz}$. To reduce this to the $\sim 400\,\text{Hz}$ required for permanent storage, an immediate suppression by a factor of $\sim 10^7$ is needed which at the same time must ensure a maximum efficiency for interesting events such as Higgs boson decays or exotic processes beyond the Standard Model. The Trigger System employed by ATLAS at $\sqrt{s} = 13\,\text{TeV}$ consists of two levels: L1 and the event filter [22]. Each step increases the number of events rejected based on various selection criteria. L1 identifies events with high transverse-momentum particles and jets from the various detector components as well as large amounts of missing and transverse energy. The selection is based on a trigger 'menu' of various combinations of trigger selections from different subsets of detectors. L1 also identifies regions of interest in a particular event and passes the coordinates of this region along with the type of event and the information on the thresholds the event filter. The event filter uses the full information from the highlighted detector areas to further reduce the number of events by performing a detailed, software based offline analysis on the remaining candidates.

4. Analysis Methods

4.1. Signal and Background Generation

In this thesis, the signal analysed is from di-Higgs production $hh \to WW^*\gamma\gamma$ by gluon fusion where one Higgs boson decays to two photons and the other to two W bosons. At the time of this thesis only non-resonant, SM, signals with $m_h = 125\,\text{GeV}$ are available, but the analysis can be easily extended to Beyond Standard Model heavy Higgs decays $H \to hh \to WW^*\gamma\gamma$ processes in the near future. For the signal, around 8000 events were generated using the **MadGraph5_ aMC@NLO** [23] Monte-Carlo event generator using the CT10 [24] PDF, while **Herwig++** [25] with the CTEQ [26] PDF was used for used for parton showering and the modelling of multi-parton interactions (MPI). The low statistics stems from the requirement for events to contain at least 1 jet with $p_\text{T} > 100\,\text{GeV}$. Very few SM di-Higgs events are expected to contain such a jet and limited computing resources prevents the production of additional high-p_T MC events.
For the background the two most relevant single Higgs production mechanisms GGF and VBF were used. They were created using the **POWHEG** [27] generator and CT10 PDF for the event generation and the **Pythia** [28] with CTEQ for the parton showering. The background mechanisms were chosen for the ability of their $h \to \gamma\gamma$ decay to mimic the photon side of the $hh \to WW^*\gamma\gamma$ channel as well as the tendency of radiated jets to recreate the WW^* topology. The choice to include both stems from the unique topology of the forward scattered jets from the VBF mechanism. An overview of the Generators and PDFs can be found in Table 4.1.

Process	# of Events	Cross Sec. [pb]	Event Gen. (PDF)	MPI(PDF)
$hh \to WW^*\gamma\gamma$	8216	-	**MadGraph5** (CT10)	**Herwig++** (CTEQ)
GGF $h \to \gamma\gamma$	6229	30.182	**POWHEG** (CT10)	**Pythia** (CTEQ)
VBF $h \to \gamma\gamma$	6637	3.8272	**POWHEG** (CT10)	**Pythia** (CTEQ)

Table 4.1.: Overview of signal and background creation using MC generation. The cross sections are commonly used in MC generation

4.2. Jet Algorithms

The calorimeter deposits discussed in Section 2.3 are not yet useful for physics analyses until they have been clustered together into physically meaningful objects. Jet algorithms use these calorimeter energy deposits from final state hadrons to create distinct, often cone-shaped entities known as jets that can be subsequently used for analysis where the constituents of each jet are thought to originate from a common source.
Jets can be produced from a variety of different inputs. Track jets involve data originating from the inner tracking chambers of the detector whereas the Local Calibration Topological Cluster (LCTopo) jets get their information purely from the calorimeters. ParticleFlow jets combine both regions. In the case of Monte-Carlo generated jet collections, all three cases require additional treatment to account for the calibrations of the specific detector in order to accurately model the real-world performance. These calibrations are not yet available and so this analysis uses truth jet collections created from stable hadrons in Monte-Carlo generated data after the implementation of hadronisation. Jet algorithms can be divided into the reconstruction algorithms used to create the original jets and the various grooming algorithms that then optimise each jet for the intended analysis. Here the various algorithms used in the main analysis are discussed.

4.2.1. Reconstruction Algorithms

A basic example of a reconstruction algorithm is the k_t family of algorithms [29]. It falls into the category of sequential recombination algorithms that have been proven to be infrared and collinear (IRC) safe. Reconstruction is based on the following definition of a distance measure d_{ij} between constituents i and j:

$$d_{ij} = \min(p_{\mathrm{T},i}^{2m}, p_{\mathrm{T},j}^{2m}) \frac{\Delta R_{ij}^2}{R^2}$$
$$d_{iB} = p_{\mathrm{T},i}^2.$$

Here $P_{\mathrm{T},i}$ denotes the transverse momentum of the i-th constituent and d_{iB} the distance between the i-th constituent and the beam. The measure

$$\Delta R_{ij} = \sqrt{(\phi_i - \phi_j)^2 + (y_i - y_j)^2}$$

gives the angular separation between the constituents in terms of the rapidity y and azimuthal angle ϕ. y has in the past been shown to be more effective than the pseudorapidity η at this stage of analysis. The general method is as follows:

1. Calculate all distances d_{ij} and d_{iB}. Find the minimum value.

2. If minimum is between constituents d_{ij}, combine them.

3. Otherwise, if minimum is d_{iB}, relabel constituent as a jet and remove it from the list of constituents.

4. Repeat until all constituents have been combined into jets.

The reconstruction is dependent on the input parameter R. This can used to determine the size of the jets created and must be determined before application of the reconstruction algorithm. A previous value of $R = 1.2$ was shown to provide good results in tagging boosted hadronic objects [30].
In addition to R, the algorithm depends on a tunable parameter, m, that determines the order in which constituents are recombined. The K_t-algorithm uses a value of $m = 1$ in the exponents of the momenta. In the past values of $m = -1$ and $m = 0$ have also been shown to be effective. These variations on the original algorithm are respectively known as the anti-K_t [31] and the the Cambridge-Aachen (C/A) [32] methods. Figure 4.1 shows a comparison of the three mentioned sequential recombination algorithms using identical inputs. It should be noted that the combination process used for C/A is entirely momenta independent focussing only on the distances between constituents, whereas the use of the inverse momenta for the anti-K_t method means that the hardest constituents tend to be combined first leading to the creation of jets with circular cones which are subsequently easier to use.

4.2.2. Grooming Algorithms

The purpose of jet grooming algorithms is to reduce contamination of the highlighted process by pile-up elsewhere in the detector and to remove soft radiation from the jets, revealing the hard, physically relevant substructure. Three different types of grooming algorithms were used on the jet collections in this analysis.

Trimming

After the initial reconstruction, subjets are constructed within the original jets using the k_t method with a radius parameter R_{sub} that is taken to be smaller than R used for the main jets [34]. These subjets are discarded if their momentum is less than a fraction of the momentum of the original jet $p_{\mathrm{T},i}/p_{\mathrm{T},jet} < f_{cut}$. The surviving subjets are then combined to form the groomed jet. Reference values are $R_{sub} = 0.2$ and $f_{cut} = 5\%$ [30].

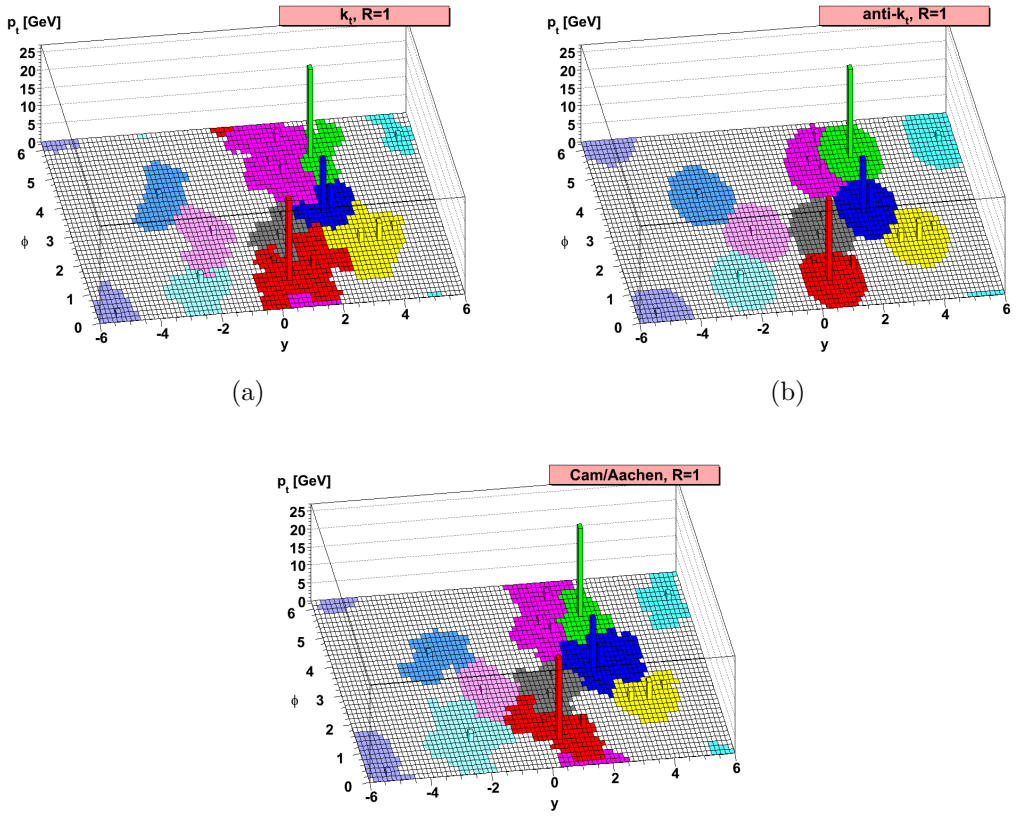

Figure 4.1.: The results of different jet algorithms [33]: (a) k_t, (b) anti-k_t, (c) Cam/Aachen.

The effects of jet trimming on pile-up can be seen in Figure 4.2 for different values of the mean number of interactions per bunch crossing μ, a value representative for the amount of pileup in the detector. Jets belonging to the background gaussian distribution have their constituents removed revealing the sharply peaked signal.

Pruning

The constituents of the jet are re-examined using the C/A algorithm as described in Section 4.2. Each pair of jets is checked for the following conditions [35]:

$$\frac{\min(p_{\mathrm{T},i}, p_{\mathrm{T},j})}{p_{\mathrm{T},p}} < z_{cut},$$
$$\Delta R_{ij} > D_{cut}.$$

$p_{\mathrm{T},p}$ is the transverse momentum of the two constituents after merging $ij \to p$. If either condition is met the jet constituent with the lower p_{T} is discarded. Otherwise the re-

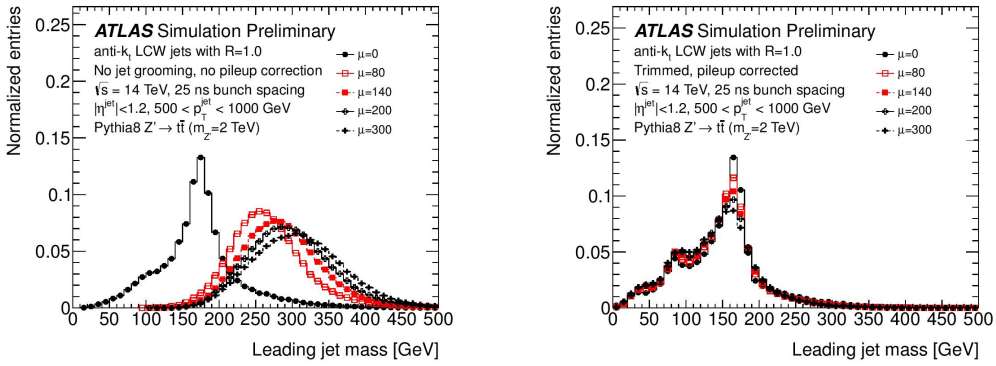

(a) (b)

Figure 4.2.: Example jet mass distribution before (a) and after (b) trimming for different mean numbers of interactions per bunch crossing μ.

construction continues as normal. The purpose of the parameter z_{cut} is to remove soft radiation while the parameter D_{cut} discards wide-angled jet constituents. A natural choice of D_{cut} is the opening angle of the jet, however this is sensitive to soft radiation around the opening. As a result it is rescaled to the parameter R_{cut} based on the ratio of jet mass m_J and transverse momentum $p_{\mathrm{T},J}$: $D_{cut} = R_{cut} \cdot 2m_J/p_{\mathrm{T},j}$. The final parameters used for jet pruning are thus z_{cut} and R_{cut}. Recommended values include $z_{cut} = 10\%$ and $R_{cut} = 0.5$ [36].

Split-Filtering

The last merging step during the construction of the jet, j, is reversed, effectively splitting the jet into two components j_1, j_2, where j_1 is chosen so that $m_{j_1} > m_{j_2}$ [37]. The asymmetry of the split is then evaluated based on the momentum balance y and the mass-drop fraction μ defined by

$$y = \frac{\min(p_{\mathrm{T},1}, p_{\mathrm{T},2})}{m_J}\Delta R_{12},$$
$$\mu = \frac{\max(m_1, m_2)}{m_J}.$$

If the conditions $y > y_{min}$ and $\mu < \mu_{max}$ are fulfilled, the jet is accepted. Otherwise the process is repeated iteratively using j_1 as the new jet j. After completion of the splitting process the remainder of the jet is reconstructed using the radius parameter $R_{sub} = \min(0.3, R_{12})$ [38].

	Reco. Alg.	R	Grooming Alg.	Parameter 1	Parameter 2
AntiKt10Trimmed	anti-k_t	1.0	Trimmed	$R_{sub} = 0.2$	$f_{cut} = 5\%$
CA10Pruned	C/A	1.0	Pruned	$z_{cut} = 15\%$	$R_{cut} = 0.5$
CA12SplitFiltered15	C/A	1.2	Split-Filtered	$y_{min} = 0.15$	$\mu_{max} = 100\%$
CA12SplitFiltered04	C/A	1.2	Split-Filtered	$y_{min} = 0.04$	$\mu_{max} = 100\%$

Table 4.2.: The truth jet collections used in the analysis. Parameters based on Section 4.2.2.

4.2.3. Introduction of Jet Collections

The truth jet collections used in the analysis are listed in Table 4.2. Included is the reconstruction algorithm used and the grooming method along with the relevant parameters. They represent a selection of some of the most common combinations used in the reconstruction of boosted W bosons [38].

4.3. Substructure Variables

Substructure variables are quantities that can be calculated for jets and used to determine the distribution of high energy constituents. The numerous types of variables can involve definitions based on the global jet properties such as jet mass and the jet axis, as well as the jet constituents and their history during jet reconstruction. The two main types used in this analysis are introduced below.

4.3.1. N-subjettiness

N-subjettiness variables [39] are given by the p_{T}-weighted sum of the angular distances between the jet constituents $i \in J$ and jet axes $a_1, ..., a_N$, predetermined by the K_t-algorithm:

$$\tau_0(\beta) = \sum_{i \in J} p_{\mathrm{T}_i} \Delta R^{\beta},$$
$$\tau_1(\beta) = \frac{1}{\tau_0(\beta)} \sum_{i \in J} p_{\mathrm{T}_i} \Delta R^{\beta}_{a_1,i},$$
$$\tau_2(\beta) = \frac{1}{\tau_0(\beta)} \sum_{i \in J} p_{\mathrm{T}_i} \mathrm{min}(\Delta R^{\beta}_{a_1,i}, \Delta R^{\beta}_{a_2,i}).$$

The measure is weighted by the sum of all transverse momenta, multiplied by the radius of the jet ΔR. The inclusion of the parameter β allows different weightings of the angular separations with $\beta = 1$ used in this analysis.

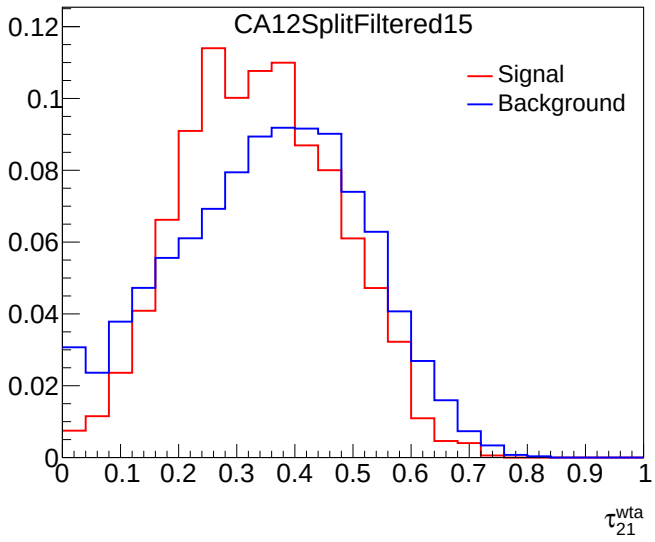

Figure 4.3.: τ_{21}^{wta} example distribution. The signal is from the on-shell W boson originating from di-Higgs production as described in Section 5.1 with jet $p_{\mathrm{T}} < 300\,\mathrm{GeV}$. The background is single Higgs production with jet $p_{\mathrm{T}} < 300\,\mathrm{GeV}$.

If a jet can be thought of as containing at least N structures, then the N-th subjettiness variable is expected to be noticeably lower than the N-1-th, and consequently the ratio $\tau_{N(N-1)} = \dfrac{\tau_N}{\tau_{N-1}}$ is a good indicator of the number of subjets contained within the primary jet with low values implying that the jet contains exactly N subjets. A slightly different version uses the hardest constituent instead of the total sum as the definition of the resulting constituent's axis during each merging in the subjet recombination algorithm. This has been shown to be more effective in some cases and is referred to as the "winner-takes-all" axis (wta-axis) [40]. For the reconstruction of the W boson from its two decay products, the following variables will be used:

$$\tau_{21} = \frac{\tau_2}{\tau_1}, \quad \tau_{21}^{wta} = \frac{\tau_2^{wta}}{\tau_1^{wta}}.$$

An example distribution can for τ_{21}^{wta} can be seen in Figure 4.3 where the signal originates from the on-shell W boson of di-Higgs production as described in Section 5.1 with jet $p_{\mathrm{T}} < 300\,\mathrm{GeV}$ and the background is single Higgs production with jet $p_{\mathrm{T}} < 300\,\mathrm{GeV}$. The signal distribution around lower τ_{21}^{wta} values implies the existence of two subjets.

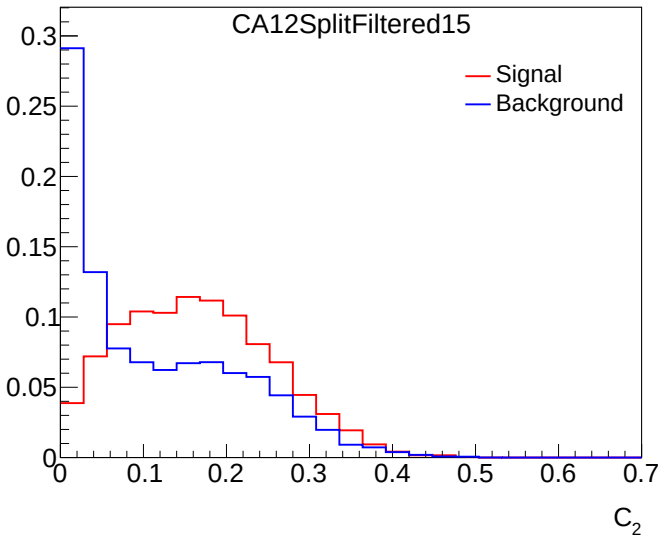

Figure 4.4.: C_2 example distribution for the on-shell W boson (Section 5.1) from di-Higgs production compared to the single Higgs background

4.3.2. Energy Correlation Ratios

The energy correlation functions are given by

$$
\begin{aligned}
E_{CF0}(\beta) &= 1, \\
E_{CF1}(\beta) &= \sum_{i \in J} P_{\mathrm{T},i}, \\
E_{CF2}(\beta) &= \sum_{i<j \in J} P_{\mathrm{T},i} P_{\mathrm{T},j} (\Delta R_{ij})^{\beta}, \\
E_{CF3}(\beta) &= \sum_{i<j<k \in J} P_{\mathrm{T},i} P_{\mathrm{T},j} P_{\mathrm{T},k} (\Delta R_{ij} \Delta R_{ik} \Delta R_{jk})^{\beta}.
\end{aligned}
$$

In contrast to the N-subjettiness variables no axes are required, instead the angular separation is between the jet constituents themselves where once again β can be used as a weight. The following ratios have proven useful in identifying jets originating from two separate energy sources [41], [42], and will be used in this analysis:

$$
C_2^{(1)} = \frac{E_{CF3}(1) \cdot E_{CF1}(1)}{(E_{CF2}(1))^2}, \qquad D_2^{(1)} = \frac{E_{CF3}(1) \cdot (E_{CF1}(1))^3}{(E_{CF2}(1))^3}.
$$

A C_2 example distribution for the on-shell W boson (Section 5.1) from di-Higgs production compared to the single Higgs background can be seen in Figure 4.4.

5. Analysis Results

The aim of this thesis is to test the efficiency of the substructure variables described in Section 5.4 in combination with different jet collections introduced in Section 4.2.3 as a means of reconstructing the boosted, on-shell, hadronically decaying W boson. To achieve this requires identification of the on-shell W decay products from truth data.

5.1. Truth Matching

The tree-level particles involved in the process $hh \to WW^*\gamma\gamma$ are as follows:

1. Two Higgs bosons h.
2. Two photons γ from $h \to \gamma\gamma$.
3. Two W bosons of which one is expected to be on-shell from $h \to WW^*$.
4. The four decay products of the W bosons.

The WW^* decay can be either fully hadronic, $qq'qq'$, fully leptonic, $\ell\nu\ell\nu$ or semi-leptonic $qq'\ell\nu$ with the branching ratios for a single W boson given in Table 5.1. Requiring that the on-shell W decay be hadronic for this analysis leads to full inclusion of the first case and full exclusion of the second case, where the particles are identified by their PDG IDs in the truth data. In the semi-leptonic case the on-shell W is first located by confirming that the invariant mass of its decay products be within 5 GeV of the known W mass, $m_W = 80.385\,\text{GeV}$ [43]. The angular separation between this Lorentz vector and the combined Lorentz vector of the qq' pair must then be smaller than that between the qq' pair and the remaining W. This is required because the MC sample used in this analysis

Decay	Branching ratio
$\ell\nu$	32.4 %
qq'	67.6 %

Table 5.1.: Branching ratios of the W boson [43].

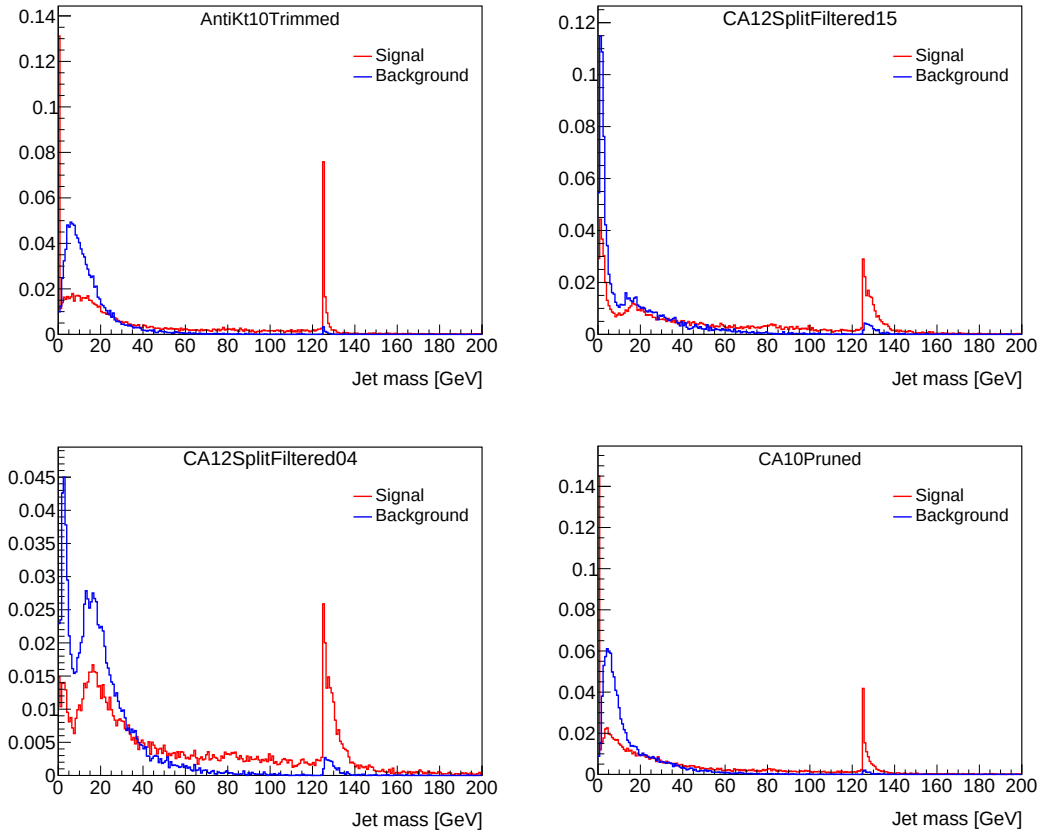

Figure 5.1.: Normalised mass distributions of the signal di-Higgs with hadronic on-shell W decay and the single Higgs background for the analysed jet collections.

does not contain the information linking each W boson to its daughter particles.
The normalised mass distributions of the signal di-Higgs with hadronic on-shell W decay and the single Higgs background from GGF and VBF can be seen in Figure 5.1. In each case the signal distribution is characterised by the resonant peak originating from the photonic decay of one of the Higgs bosons.
The evaluation of the W boson reconstruction efficiency requires a definition of said boson based on the observed jets. Only then can the substructure variables be analysed for their ability to pick out these jets from the underlying background. For this reason, the following conditions must be satisfied for jets to be associated to the W boson:

1. $\Delta R < 0.5$ with ΔR the angular distance between the jet and the W boson as determined from truth information.
2. $\frac{p_{\mathrm{T,jet}}}{p_{\mathrm{T,W}}} > 0.9$ where $p_{\mathrm{T,jet}}$ is the transverse momentum of the jet and $p_{\mathrm{T,W}}$ that of the truth W boson.

The justification for this decision can be seen in Figure 5.2 which shows the distribution

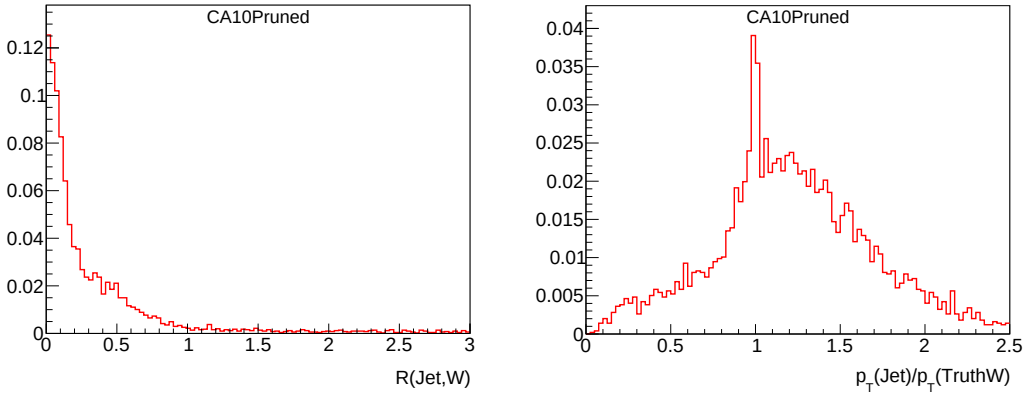

(a) (b)

Figure 5.2.: (a) Smallest angular separation between jet and W boson on an event basis. (b) Ratio between transverse momentum of jet and W boson for jet closest to W boson.

Jet collection	ξ
AntiKt10Trimmed	71.1%
CA12SplitFiltered15	65.9%
CA12SplitFiltered04	71.1%
CA10Pruned	70.8%

Table 5.2.: Percentage of events fulfilling the truth matching criteria ξ for the studied jet collections as defined in Table 4.2.

of the angular separation, ΔR, between the jet closest to the truth W boson and the truth W boson itself for one jet collection on an event basis which peaks at small values of ΔR. Also shown is the $p_{\mathrm{T,jet}}/p_{\mathrm{T,W}}$ ratio distribution for the jet closest to the W. The results are similar for the other jet collections and show that the majority of events contain a jet that is approximately collinear to the truth level particle. The motivation for the lack of an upper limit concerning the momenta ratio can also be seen. Whereas the ratio experiences a sharp peak at unity, a large proportion of events contain harder jets that are presumably constructed from both overlapping W bosons or are a result of pileup contamination. For this reason only the lower cut, $p_{\mathrm{T,jet}}/p_{\mathrm{T,W}} > 0.9$, was used. As documented in Table 5.2 the jet W matching efficiency ξ, defined as the percentage of events that fulfil the above criteria, is around 70% for all jet collections. The new mass distributions where the signal only includes the on-shell W boson decay products according to the above definition are shown in Figure 5.3 for all jet collections. Here the invariant mass distribution of the signal is broadly distributed around the mass of the W boson. The original peak at 125 GeV is significantly reduced, implying that it originated

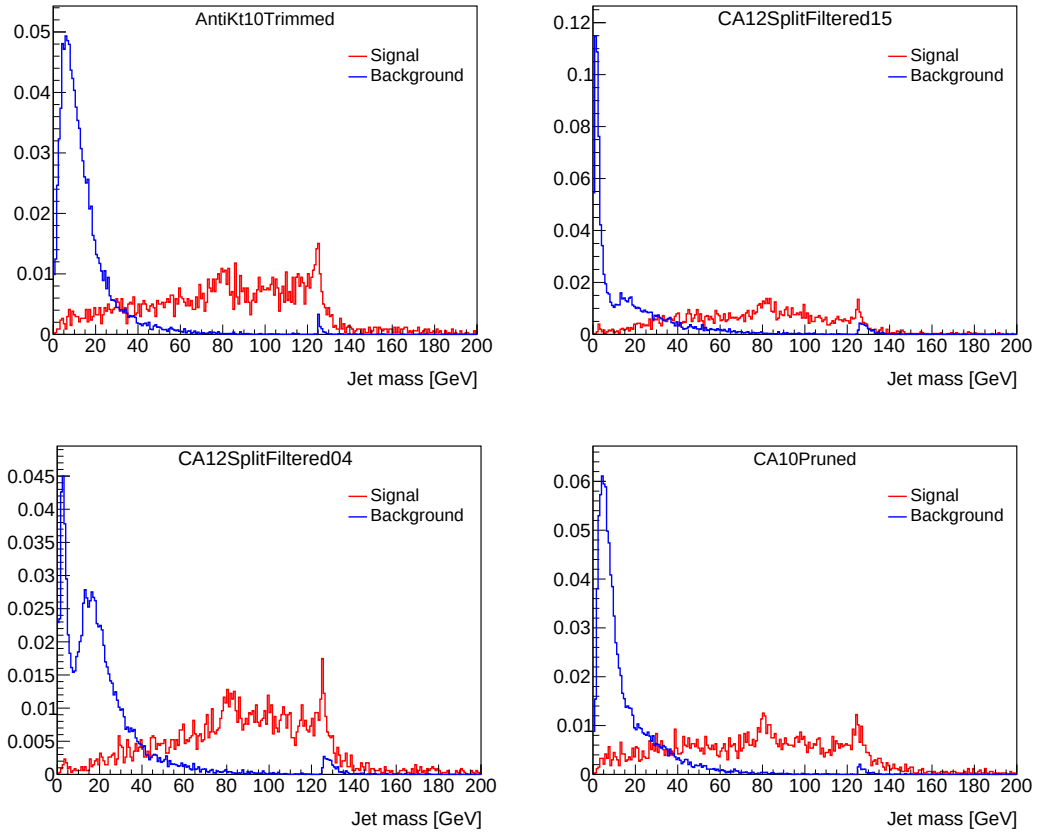

Figure 5.3.: Normalised mass distributions of the on-shell W boson decay products and the single Higgs background for the analysed jet collections.

from the two photons, as any jets from the overlapping, boosted W bosons are expected to pass the above criteria. Future analysis should thus focus on implementing photon/jet overlap removal. The lack of a clear peak at the W boson mass stems from the effects of pileup and possible overlap with the W^*. This subset is used as the signal for the following analysis.

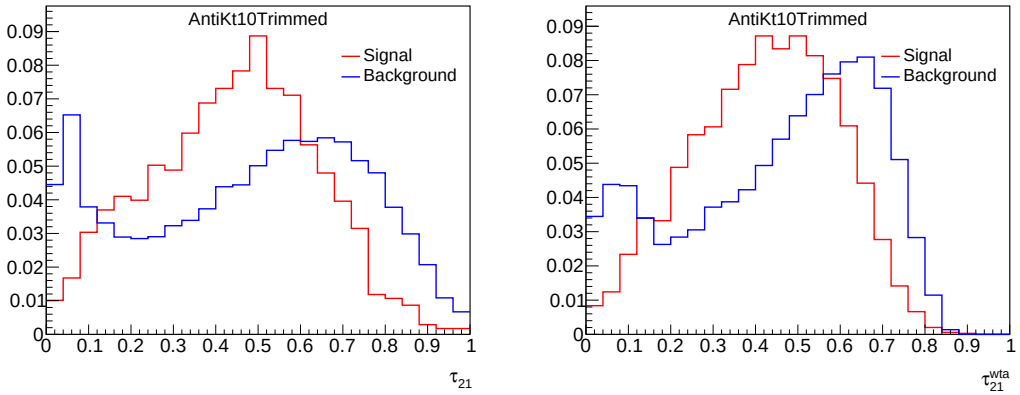

(a)

(b)

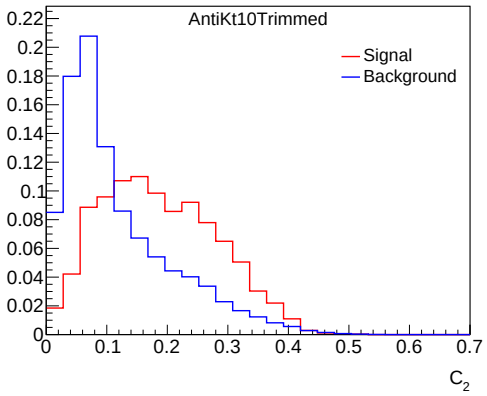

(c)

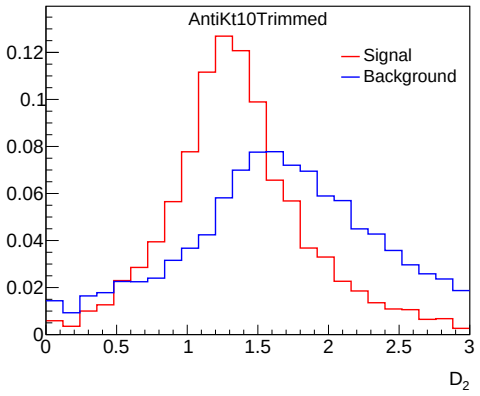

(d)

Figure 5.4.: Distribution of substructure variables for the AntiKt10Trimmed jet collection: (a) τ_{21}, (b) τ_{21}^{wta}, (c) C_2, (d) D_2.

5.2. Analysis of Substructure Distributions

With the signal clearly defined, the aim of this thesis is to identify selection criteria based on substructure variables that optimally retain jets from the signal process while suppressing jets from the VBF and GGF $h \to \gamma\gamma$ background processes.

The approach varies based on a case-by-case analysis of each substructure distribution. Figure 5.4 shows the distributions of all studied substructure variables for the AntiKt10Trimmed jet collection after truth selection. The signal efficiency ϵ_{sig} for a given cut on the substructure variable is defined as the integral of the signal distribution with applied cuts over the integral of the entire distribution:

$$\epsilon_{sig} = \frac{\int_{x_{low}}^{x_{high}} f(x)\,\mathrm{d}x}{\int f(x)\,\mathrm{d}x}$$

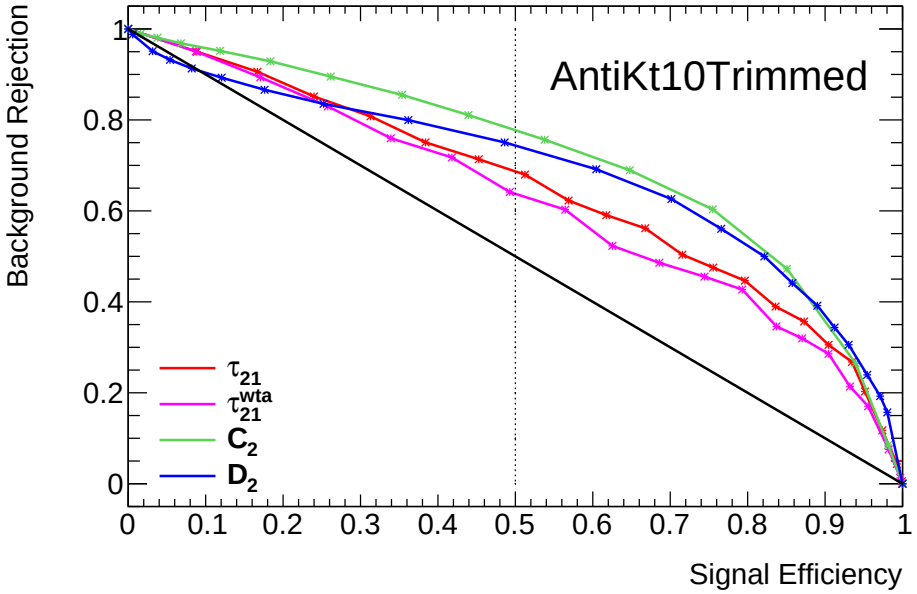

Figure 5.5.: ROC curve showing the signal efficiency versus background rejection for the AntiKt10Trimmed jet collection for all substructure variables.

where $f(x)$ represents the distribution of a particular substructure variable $x \in \{\tau_{21}, \tau_{21}^{wta}, C_2, D_2\}$ and x_{low}, x_{high} are respectively the lower and upper cuts on the substructure variable. The background efficiency ϵ_{bkg} is defined analogously.

A variation of x_{low} and x_{high} leads to the creation of multiple points $(\epsilon_{sig}, \epsilon_{bkg})$ that can be plotted on a Receiver Operating Characteristic (ROC) curve. The result for the AntiKt10Trimmed jet collection from above can be seen in Figure 5.5 where the background rejection is given by $1 - \epsilon_{bkg}$. The ROC curves for the other jet collections and the associated substructure variable distributions are listed in Appendix A.

The acquisition method for the set of x_{low} and x_{high} used to obtain the data points in the ROC curve differ depending on the relative shapes of the signal and background distributions. For cases where the signal distribution is displaced to the left of the background distribution, no lower limit is imposed, ($x_{low} = 0$), and the upper limit scans the entire range in steps corresponding to the bin size used in the histograms (left acquisition method). Conversely, for a signal that is displaced to the right, no upper limit is chosen, and the lower limit is varied (right acquisition method). In the remainder of cases where the signal distribution is shown to peak in the middle of the background distribution, both initial cut-off values are set to contain the single bin with the largest signal. For each new data point the integration range is then expanded by one bin either to the left or right such that the bin with the larger signal of the two is chosen (centre acquisition method). Although there are many more possible methods, the ones chosen here are sim-

ple and have been found to work sufficiently well allowing the identification of the optimal cut-off values x_{low}, x_{high} that simultaneously maximise signal acceptance and background rejection.
Two criteria are used for the evaluation of each variables performance:

1. The area under the ROC curve.

2. The background rejection at a fixed signal efficiency of $\epsilon_{sig} = 0.5$.

The calculation of the former is achieved by approximating the area between data points with straight lines and performing an integral on the resulting curve. For the latter, the approximation involves linear interpolation from the two data points adjacent to the 0.5 efficiency mark. The same approach is used to calculate the cut-off values that are recommended in order to obtain the same efficiency. The values for all jet collections and substructure variables are listed in Table 5.3.
Evaluating the results using the rejection at 0.5 efficiency, the standard τ_{21} variable is shown to offer a $2-5\%$ higher rejection rate compared to the τ_{21}^{wta} version. In nearly all cases the energy correlation function ratios outperform the N-subjettiness variables by up to 15% rejection.
In terms of the jet collections, the AntiKt10Trimmed version consistently provides good results varying from a $64-78\%$ rejection rate. The overall best combination, however is the CA10Pruned jet collection with the D_2, where an upper cut-off value of 1.26 is expected to obtain an $86.4 \pm 0.09\%$ background rejection rate at 50% signal efficiency The ROC curve for the CA10Pruned jet collection is shown in Figure 5.6 along with the distribution of D_2 in Figure 5.7.

5.3. $\mathbf{p_T}$ Dependent Analysis

The analysis of the previous section is repeated here on low- and high-p_{T} jets independently. Based on the distribution of the signal p_{T}, shown for the AntiKt10Trimmed jet collection in Figure 5.8, all jets from signal and background were divided into two categories with $p_{\mathrm{T}} < 300\,\mathrm{GeV}$ and $p_{\mathrm{T}} \geq 300\,\mathrm{GeV}$. The results allow the individual treatment of the two ranges, ideally enhancing the possibility of the W boson reconstruction. Higher p_{T} ranges correspond to highly boosted WW^* systems with narrower jets emanating from a hh system with a heavier invariant mass. Therefore jet p_{T} could conceivably be used as an additional selection criteria.

AntiKt10Trimmed				
	τ_{21}	τ_{21}^{wta}	C_2	D_2
Acquisition method	centre	centre	right	left
Area under ROC curve	0.65	0.62	0.72	0.69
Rejection@0.5 efficiency	0.687±0.009	0.638±0.009	0.777±0.009	0.744±0.009
x_{low}@0.5 efficiency	0.33	0.36	0.18	-
x_{high}@0.5 efficiency	0.60	0.60	-	1.33
CA12SplitFiltered15				
	τ_{21}	τ_{21}^{wta}	C_2	D_2
Acquisition method	centre	centre	right	centre
Area under ROC curve	0.56	0.57	0.67	0.56
Rejection@0.5 efficiency	0.608±0.009	0.590±0.009	0.682±0.009	0.570±0.009
x_{low}@0.5 efficiency	0.27	0.24	0.16	0.98
x_{high}@0.5 efficiency	0.48	0.44	-	1.32
CA12SplitFiltered04				
	τ_{21}	τ_{21}^{wta}	C_2	D_2
Acquisition method	centre	centre	right	left
Area under ROC curve	0.60	0.57	0.61	0.64
rejection@0.5 efficiency	0.630±0.009	0.591±0.009	0.626±0.009	0.686±0.009
x_{low}@0.5 efficiency	0.32	0.34	0.21	-
x_{high}@0.5 efficiency	0.56	0.56	-	1.29
CA10Pruned				
	τ_{21}	τ_{21}^{wta}	C_2	D_2
Acquisition method	centre	centre	right	left
Area under ROC curve	0.64	0.61	0.65	0.80
Rejection@0.5 efficiency	0.653±0.009	0.621±0.009	0.711±0.009	0.864±0.009
x_{low}@0.5 efficiency	0.32	0.31	0.16	-
x_{high}@0.5 efficiency	0.59	0.56	-	1.26

Table 5.3.: Table showing recommended cut-off parameters x_{low} and x_{high}, total area under ROC curve, and expected background rejection at 0.5 efficiency for all jet collections and substructure variables. The rejection efficiency errors are statistical only.

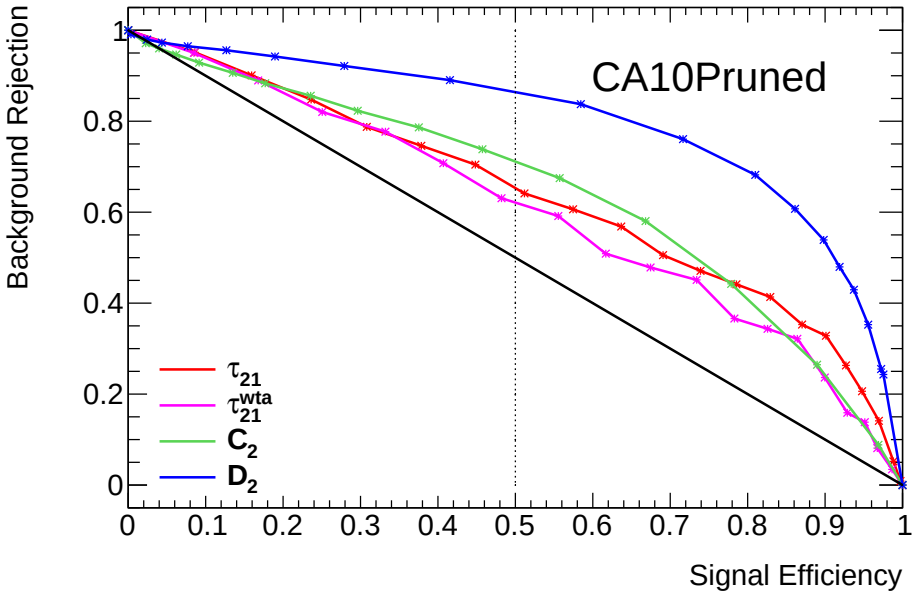

Figure 5.6.: ROC curve for the CA10Pruned jet collection showing the D_2 variable as the optimal case.

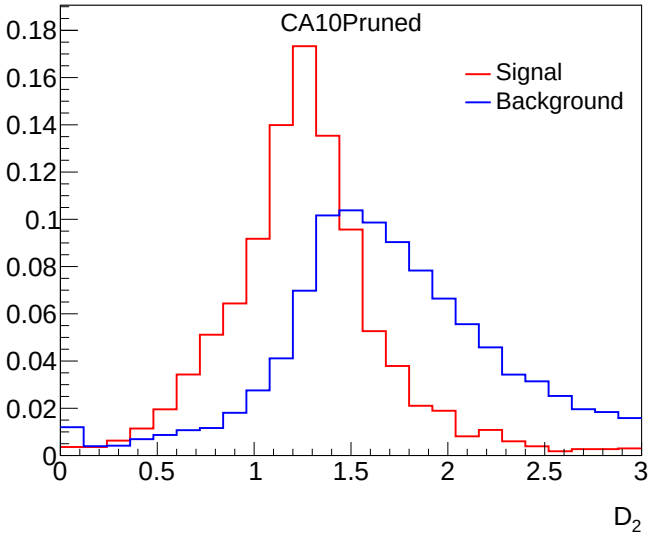

Figure 5.7.: Distribution of the D_2 substructure variable with the CA10Pruned jet collection.

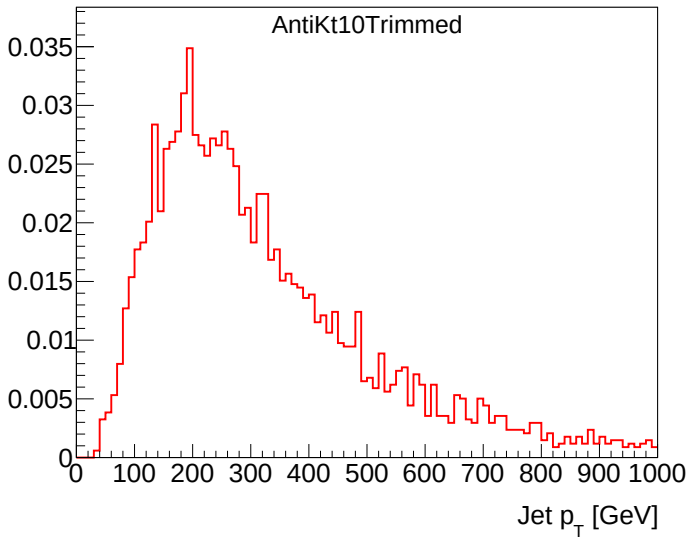

Figure 5.8.: Distribution of the signal p_{T} for the AntiKt10Trimmed jet collection, motivating the decision to divide the signal into two equally sized categories, $p_{\mathrm{T}} < 300\,\mathrm{GeV}$ and $p_{\mathrm{T}} \geq 300\,\mathrm{GeV}$.

5.3.1. $\mathbf{p_{\mathrm{T}} < 300\,GeV}$

The ROC curve and substructure variable distributions for the AntiKt10Trimmed jet collection are shown in Figures 5.9 and 5.10 and the results are documented in Table 5.4. Results from the remaining jet collections can be found in Appendix B.
At low-p_{T}, the background rejection at 50% signal efficiency is shown to be minimally higher than in the inclusive p_{T} case. The difference is most noticeable for the energy correlation ratios that reject up to 15% more of the background compared the to the N-subjettiness variables and up to 8% more of the background compared to the inclusive p_{T} case. The recommended combination remains the CA10Pruned jet collection and the D_2 variable with an upper limit of 1.26 shown in Figures 5.11 and 5.12. The expected background rejection is $86.8 \pm 1.2\%$.

5.3.2. $\mathbf{p_{\mathrm{T}} \geq 300\,GeV}$

As can be seen in Figure 5.14 the distributions of the substructure variables at high-p_{T} differ strongly from those at low-p_{T}. In all cases the background is characterized by a sharp peak at very low values allowing the use of a lower cut-off value for each substructure variable. This results in background rejection rates of over 80% for nearly all variables with little difference between the two different types. Similarly, there is little to distinguish between the four jet algorithms. The best performance is achieved with the C_2 variable

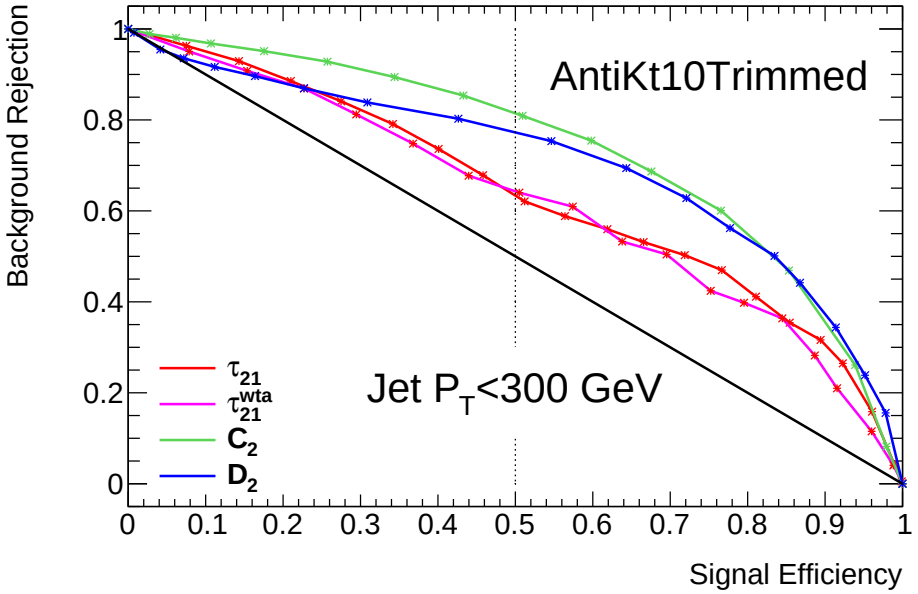

Figure 5.9.: ROC curve showing the signal efficiency versus background rejection for the AntiKt10Trimmed jet collection with $p_{\mathrm{T}} < 300\,\mathrm{GeV}$ for all substructure variables.

and the AntiKt10Trimmed jet collection (see Figure 5.13) which rejects $94.4 \pm 1.3\%$ of the background at 50% signal efficiency (Table 5.5). Results from the other jet collections can be found in Appendix C.

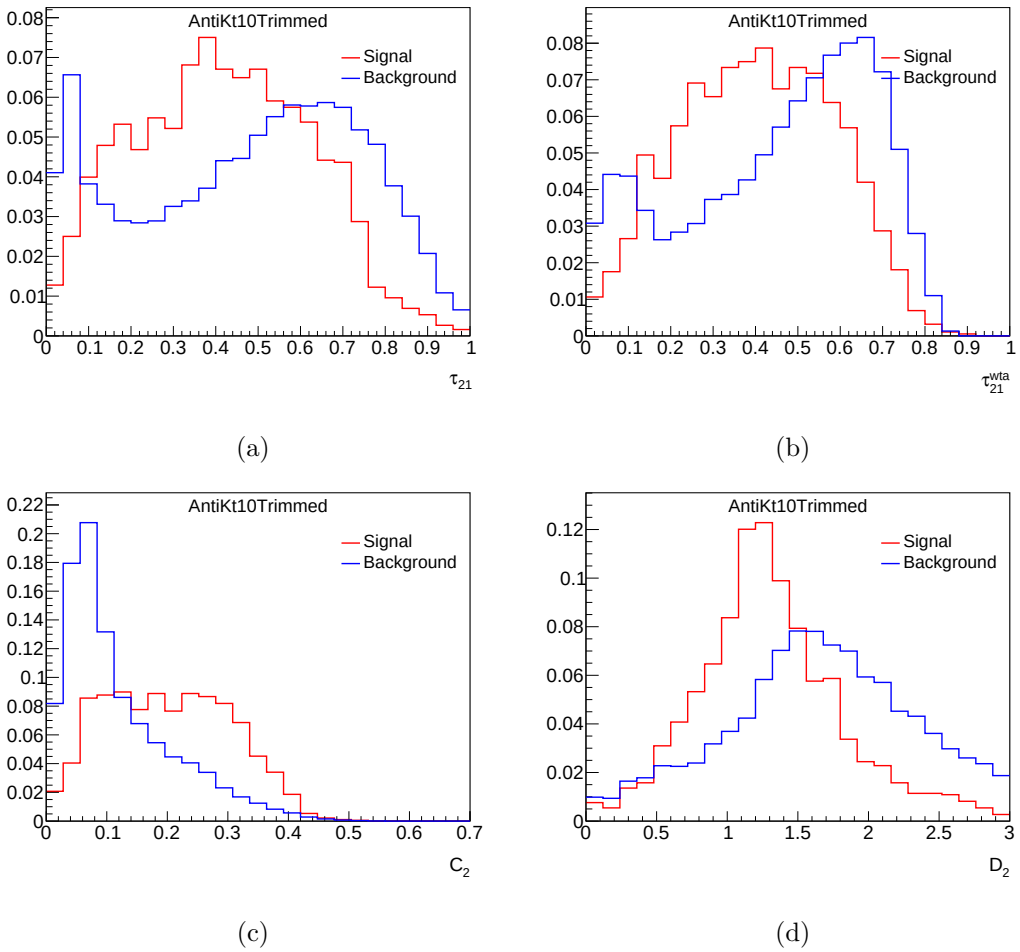

Figure 5.10.: Substructure Distribution functions for the AntiKt10Trimmed jet collection with $p_{\mathrm{T}} < 300\,\mathrm{GeV}$: (a) τ_{21}, (b) τ_{21}^{wta}, (c) C_2, (d) D_2.

AntiKt10Trimmed				
	τ_{21}	τ_{21}^{wta}	C_2	D_2
Acquisition method	centre	centre	right	left
Area under ROC curve	0.64	0.62	0.74	0.71
Rejection@0.5 efficiency	0.634±0.012	0.643±0.012	0.814±0.012	0.772±0.012
x_{low}@0.5 efficiency	0.32	0.28	0.20	-
x_{high}@0.5 efficiency	0.63	0.56	-	1.27
CA12SplitFiltered15				
	τ_{21}	τ_{21}^{wta}	C_2	D_2
Acquisition method	centre	centre	right	centre
Area under ROC curve	0.60	0.59	0.73	0.56
Rejection@0.5 efficiency	0.631±0.012	0.624±0.012	0.762±0.012	0.571±0.012
x_{low}@0.5 efficiency	0.24	0.21	0.20	0.96
x_{high}@0.5 efficiency	0.45	0.40	-	1.30
CA12SplitFiltered04				
	τ_{21}	τ_{21}^{wta}	C_2	D_2
Acquisition method	centre	centre	right	left
Area under ROC curve	0.60	0.57	0.67	0.67
rejection@0.5 efficiency	0.642±0.012	0.579±0.012	0.710±0.012	0.729±0.012
x_{low}@0.5 efficiency	0.28	0.29	0.24	-
x_{high}@0.5 efficiency	0.52	0.52	-	1.24
CA10Pruned				
	τ_{21}	τ_{21}^{wta}	C_2	D_2
Acquisition method	centre	centre	right	left
Area under ROC curve	0.63	0.59	0.70	0.79
Rejection@0.5 efficiency	0.652±0.012	0.603±0.012	0.775±0.012	0.868±0.012
x_{low}@0.5 efficiency	0.26	0.29	0.19	-
x_{high}@0.5 efficiency	0.56	0.55	-	1.26

Table 5.4.: Table showing recommended cut-off parameters x_{low} and x_{high}, total area under ROC curve, and expected background rejection at 0.5 efficiency for all jet collections with $p_{\mathrm{T}} < 300\,\mathrm{GeV}$ and all substructure variables. The rejection efficiency errors are statistical only.

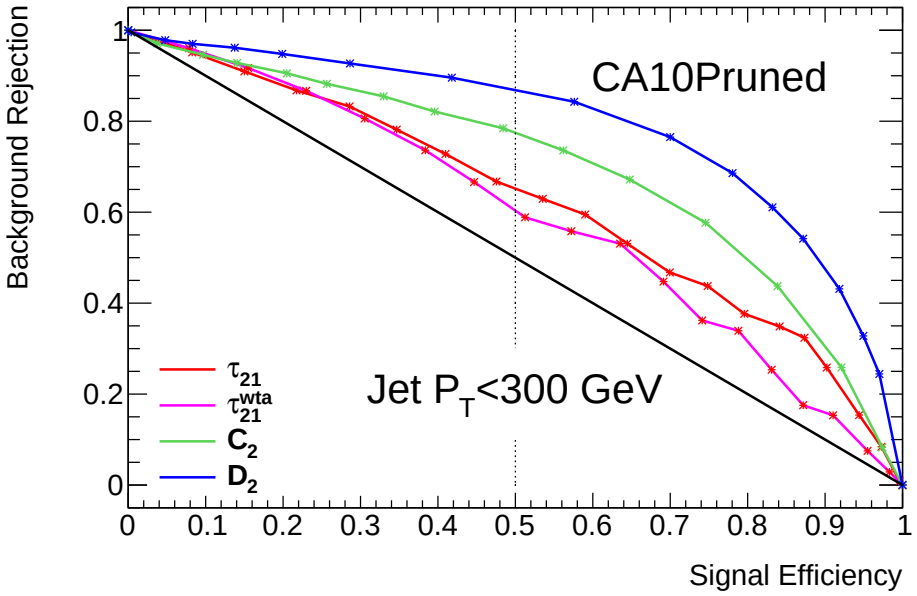

Figure 5.11.: ROC curve for the CA10Pruned jet collection at $p_{\mathrm{T}} < 300\,\mathrm{GeV}$ showing the D_2 variable as the optimal case.

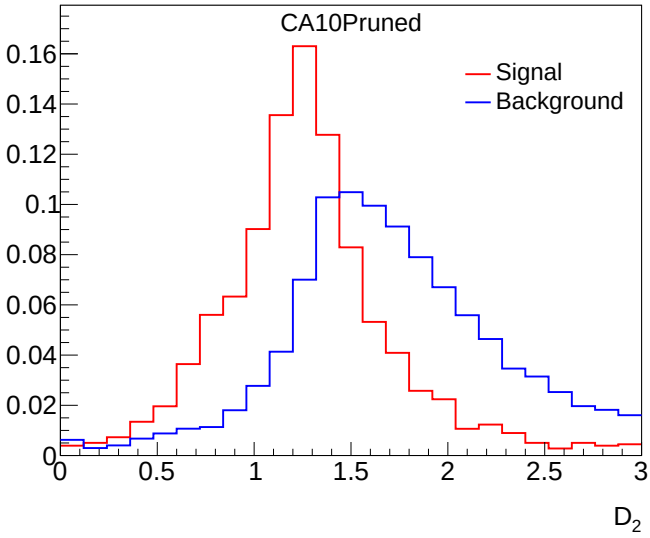

Figure 5.12.: Distribution of the D_2 substructure variable with the CA10Pruned jet collection at $p_{\mathrm{T}} < 300\,\mathrm{GeV}$.

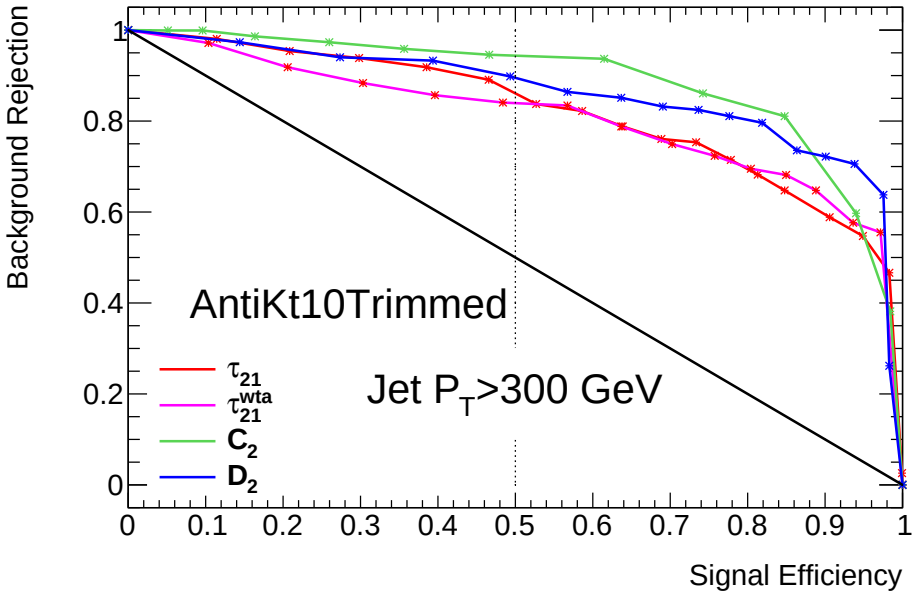

Figure 5.13.: ROC curve showing the signal efficiency versus background rejection for the AntiKt10Trimmed jet collection with $p_T > 300\,\text{GeV}$ for all substructure variables.

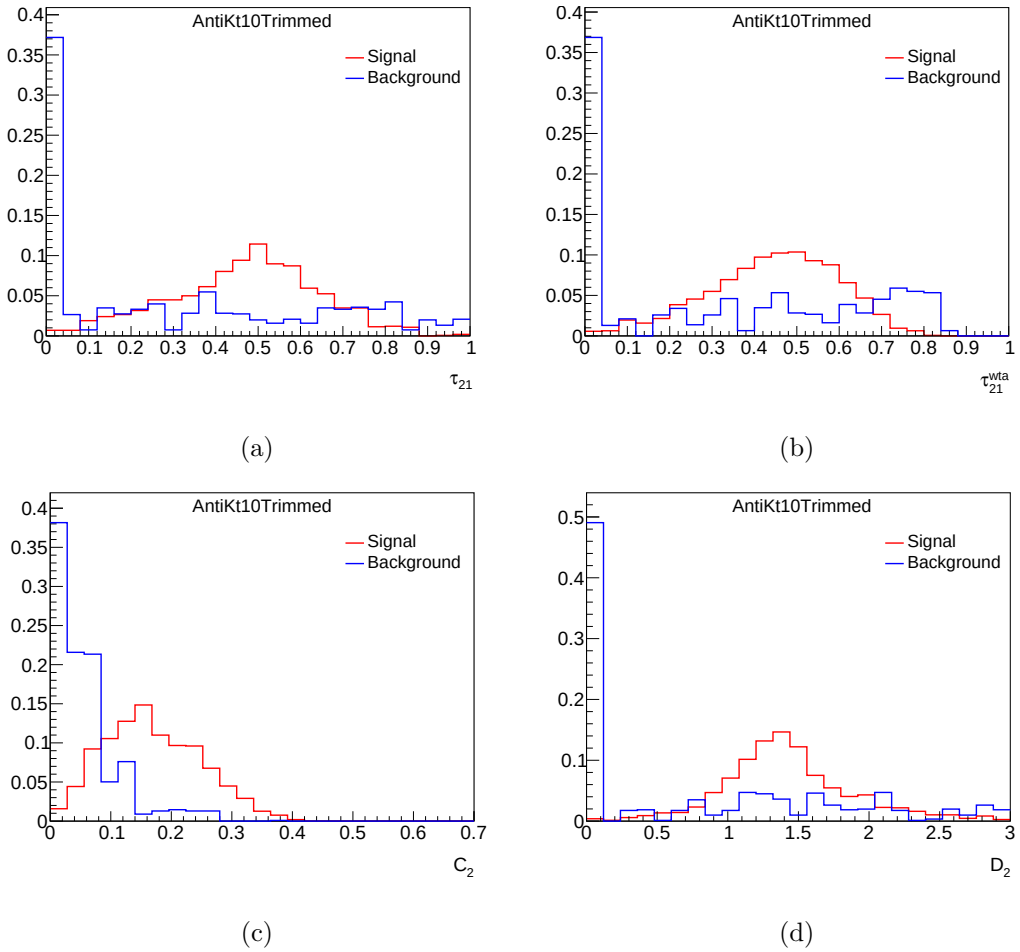

Figure 5.14.: Substructure Distribution functions for the AntiKt10Trimmed jet collection with $p_{\mathrm{T}} \geq 300\,\mathrm{GeV}$: (a) τ_{21}, (b) τ_{21}^{wta}, (c) C_2, (d) D_2.

AntiKt10Trimmed				
	τ_{21}	τ_{21}^{wta}	C_2	D_2
Acquisition method	centre	centre	right	centre
Area under ROC curve	0.82	0.81	0.89	0.86
Rejection@0.5 efficiency	0.861±0.013	0.839±0.013	0.944±0.013	0.895±0.013
x_{low}@0.5 efficiency	0.38	0.39	0.16	1.08
x_{high}@0.5 efficiency	0.60	0.60	-	1.57
CA12SplitFiltered15				
	τ_{21}	τ_{21}^{wta}	C_2	D_2
Acquisition method	right	right	right	right
Area under ROC curve	0.84	0.83	0.83	0.82
Rejection@0.5 efficiency	0.868±0.014	0.858±0.014	0.883±0.014	0.815±0.014
x_{low}@0.5 efficiency	0.38	0.37	0.12	1.18
x_{high}@0.5 efficiency	-	-	-	-
CA12SplitFiltered04				
	τ_{21}	τ_{21}^{wta}	C_2	D_2
Acquisition method	right	right	right	right
Area under ROC curve	0.83	0.80	0.84	0.75
Rejection@0.5 efficiency	0.888±0.013	0.832±0.013	0.875±0.013	0.763±0.013
x_{low}@0.5 efficiency	0.47	0.45	0.17	1.36
x_{high}@0.5 efficiency	-	-	-	-
CA10Pruned				
	τ_{21}	τ_{21}^{wta}	C_2	D_2
Acquisition method	centre	centre	right	centre
Area under ROC curve	0.85	0.83	0.86	0.87
Rejection@0.5 efficiency	0.870±0.013	0.846±0.013	0.915±0.013	0.918±0.013
x_{low}@0.5 efficiency	0.36	0.32	0.13	1.08
x_{high}@0.5 efficiency	0.60	0.54	-	1.48

Table 5.5.: Table showing recommended cut-off parameters x_{low} and x_{high}, total area under ROC curve, and expected background rejection at 0.5 efficiency for all jet collections with $p_T \geq 300\,\text{GeV}$ and all substructure variables. The rejection efficiency errors are statistical only.

6. Conclusion

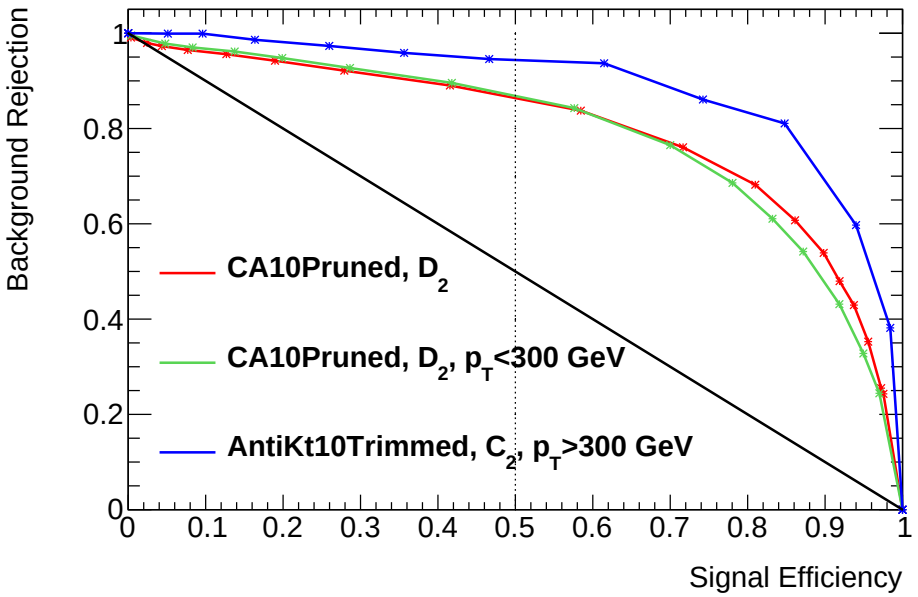

Figure 6.1.: ROC curve showing the optimal combination of jet collection and substructure variable for each p_{T} range.

In this thesis, a combination of commonly used jet collections and substructure variables were evaluated for their ability to reconstruct the boosted, hadronically decaying, on-shell W boson from SM $hh \to WW^*\gamma\gamma$ processes over different p_{T} ranges. Although the accuracy of the results are heavily limited by statistics and future research is needed to narrow down the precise parameters for the jet collections, a number of results can be obtained from the data:

1. As could have been expected, the best reconstruction is possible with high-p_{T} jets. In particular, in this range the background samples from single Higgs bosons are dominated by jets with very low substructure variable values, resulting in lower cut-offs that exclude large amounts of the background.

2. The CA12SplitFiltered15 and CA12SplitFiltered04 jet collections return worse results than the other two analysed jet collections. It is unclear if this is due to the

p_{T} range	Jet collection	Substr. Var.	Rejection (0.5 eff.)	x_{low}	x_{high}
Inclusive	CA10Pruned	D_2	0.864±0.009	-	1.26
$p_{\mathrm{T}} < 300\,\mathrm{GeV}$	CA10Pruned	D_2	0.868±0.012	-	1.26
$p_{\mathrm{T}} > 300\,\mathrm{GeV}$	AntiKt10Trimmed	C_2	0.944±0.013	1.62	-

Table 6.1.: Recommended cut-off values for optimal W boson reconstruction in each analysed p_{T} range.

Split-Filtering Algorithms or if the jet reconstruction parameter $R = 1.2$ is too large for reconstruction of the W boson.

3. The energy correlation ratios C_2 and D_2 are to be preferred over the N-subjettiness variables, τ_{21} and τ_{21}^{wta}. This is in line with previous studies showing their effectiveness in evaluating jet substructure [41], [42].

4. In the inclusive and lower p_{T} ranges the C_2 signal distribution tends to lie to the right of the background distribution whereas th D_2 distribution mostly lies to the left. This raises the possibility of combining the two to approach the signal from both directions and greatly increase reconstruction efficiency.

Finally, the best reconstruction method is plotted for each p_{T} range in Figure 6.1. The jet collection, substructure variable and cut-offs used are shown in Table 6.1.
Future research should focus on refining the choice of jet collection as well as including the calibrations for the other jet input types on reconstructed level jets. This will better model the performance of the ATLAS detector in preparation for the large amounts of real data currently being produced.
The results obtained in this analysis are expected to be heavily dependent on the invariant mass of the system. As a result the method should be repeated for the BSM, resonant $H \to hh$ case for a variety of heavy Higgs masses. This will allow for optimal evaluation of any unexpected signal seen by the ATLAS detector in this channel in the coming years.

A. ROC Curves and Substructure Distributions: Inclusive p_T

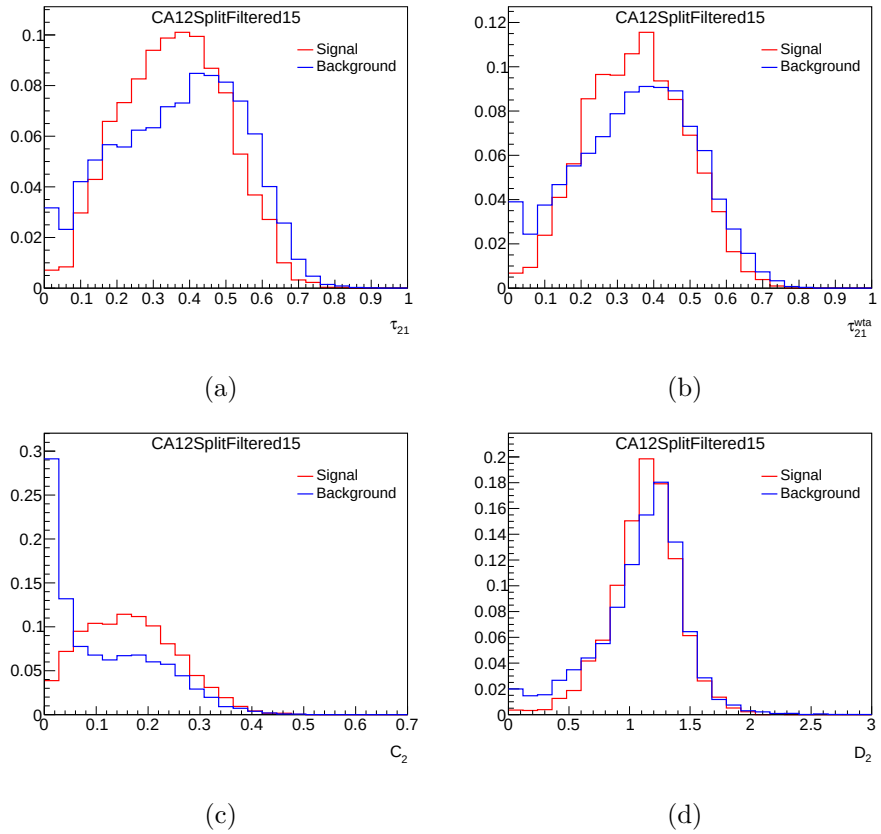

Figure A.1.: Substructure Distribution functions for the CA12SplitFiltered15 jet collection: (a) τ_{21}, (b) τ_{21}^{wta}, (c) C_2, (d) D_2.

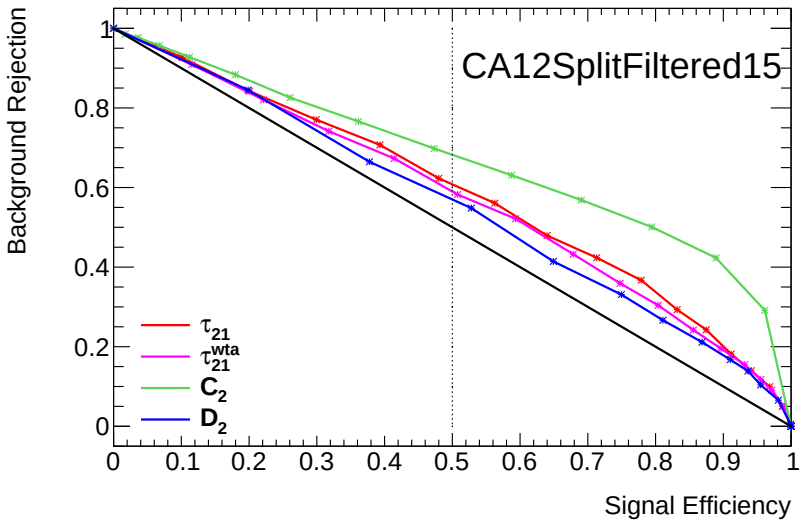

Figure A.2.: ROC curve showing the signal efficiency versus background rejection for the CA12SplitFiltered15 jet collection for all substructure variables.

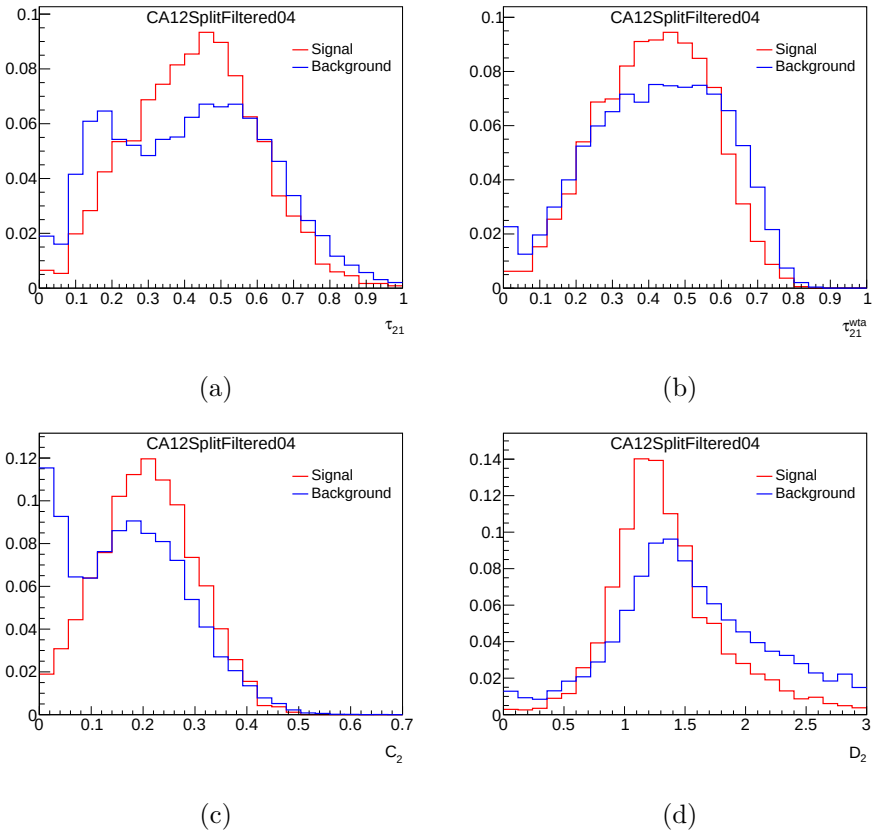

Figure A.3.: Substructure Distribution functions for the CA12SplitFiltered04 jet collection: (a) τ_{21}, (b) τ_{21}^{wta}, (c) C_2, (d) D_2.

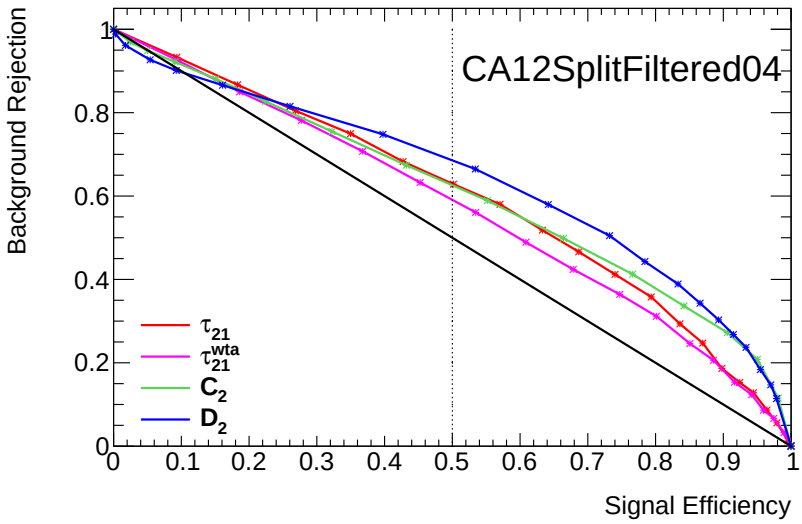

Figure A.4.: ROC curve showing the signal efficiency versus background rejection for the CA12SplitFiltered04 jet collection for all substructure variables.

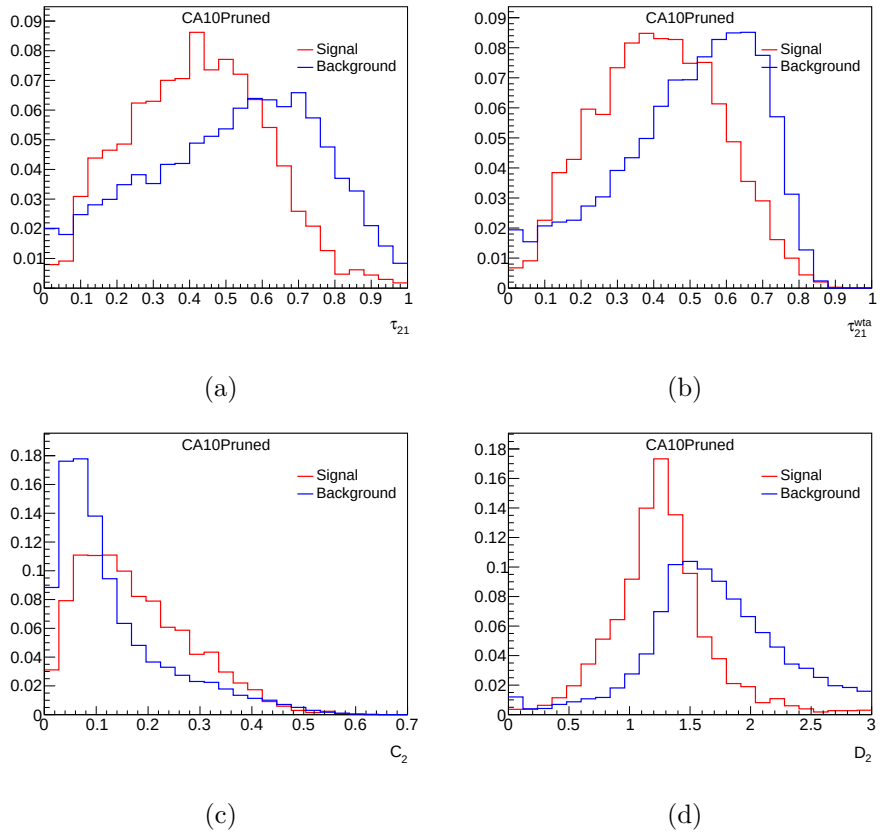

Figure A.5.: Substructure Distribution functions for the CA10Pruned jet collection: (a) τ_{21}, (b) τ_{21}^{wta}, (c) C_2, (d) D_2.

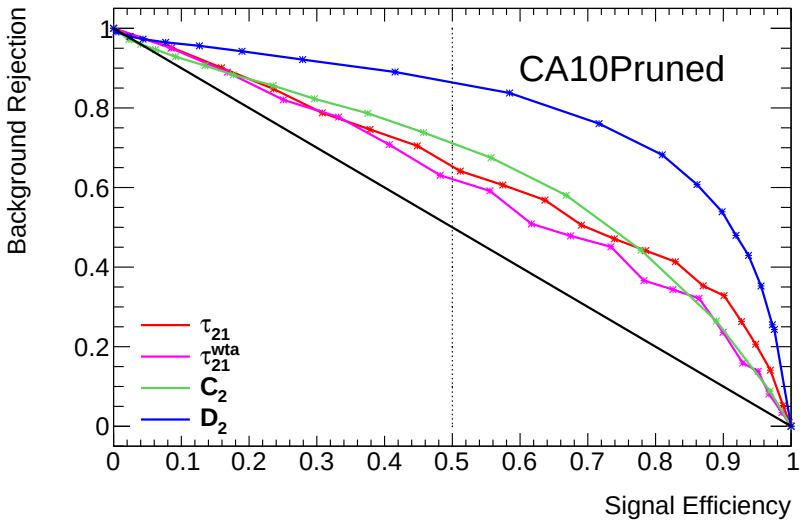

Figure A.6.: ROC curve showing the signal efficiency versus background rejection for the CA10Pruned jet collection for all substructure variables.

B. ROC Curves and Substructure Distributions: Exclusive $p_T < 300\,\mathrm{GeV}$

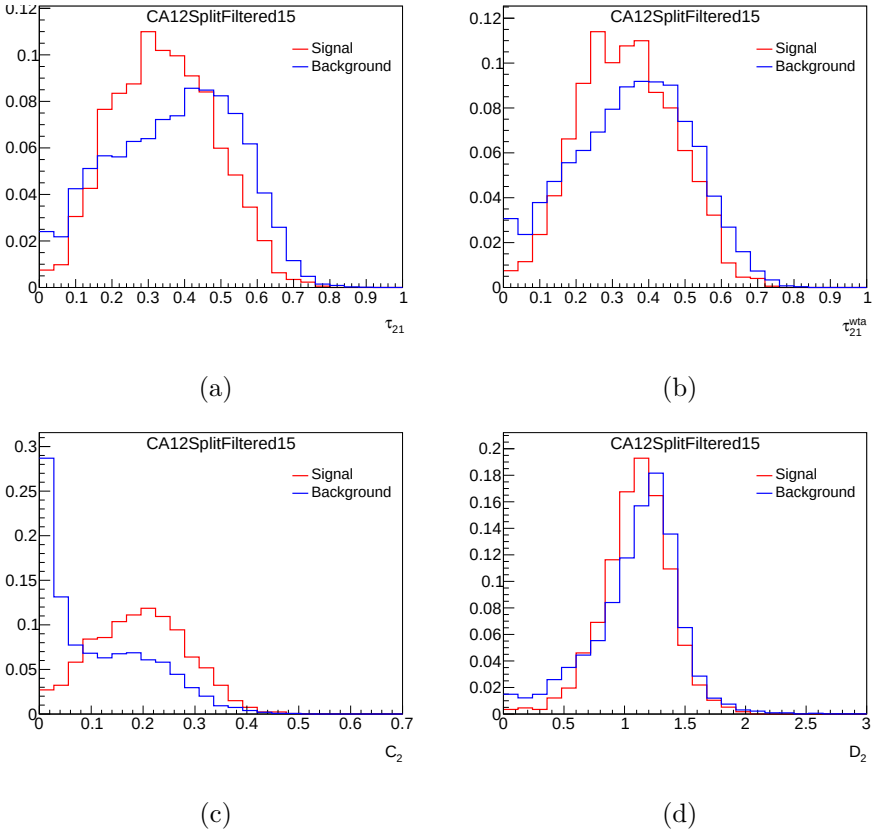

Figure B.1.: Substructure Distribution functions for the CA12SplitFiltered15 jet collection with $p_T < 300\,\text{GeV}$: (a) τ_{21}, (b) τ_{21}^{wta}, (c) C_2, (d) D_2.

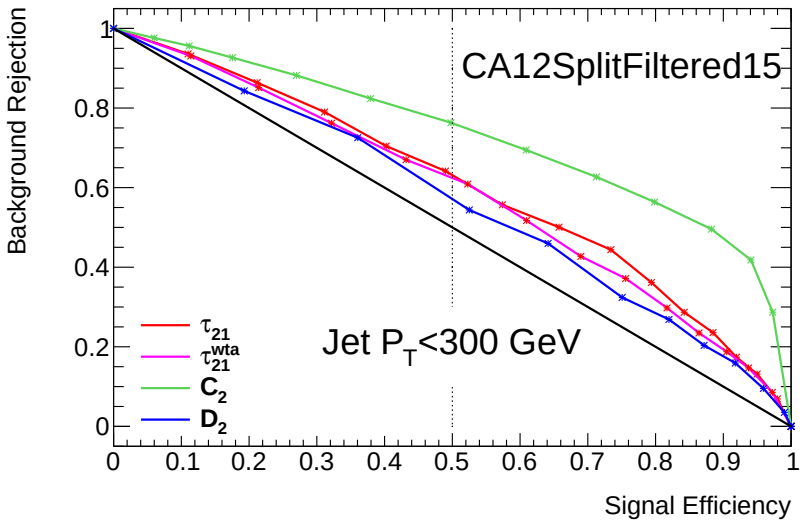

Figure B.2.: ROC curve showing the signal efficiency versus background rejection for the CA12SplitFiltered15 jet collection with $p_T < 300\,\text{GeV}$ for all substructure variables.

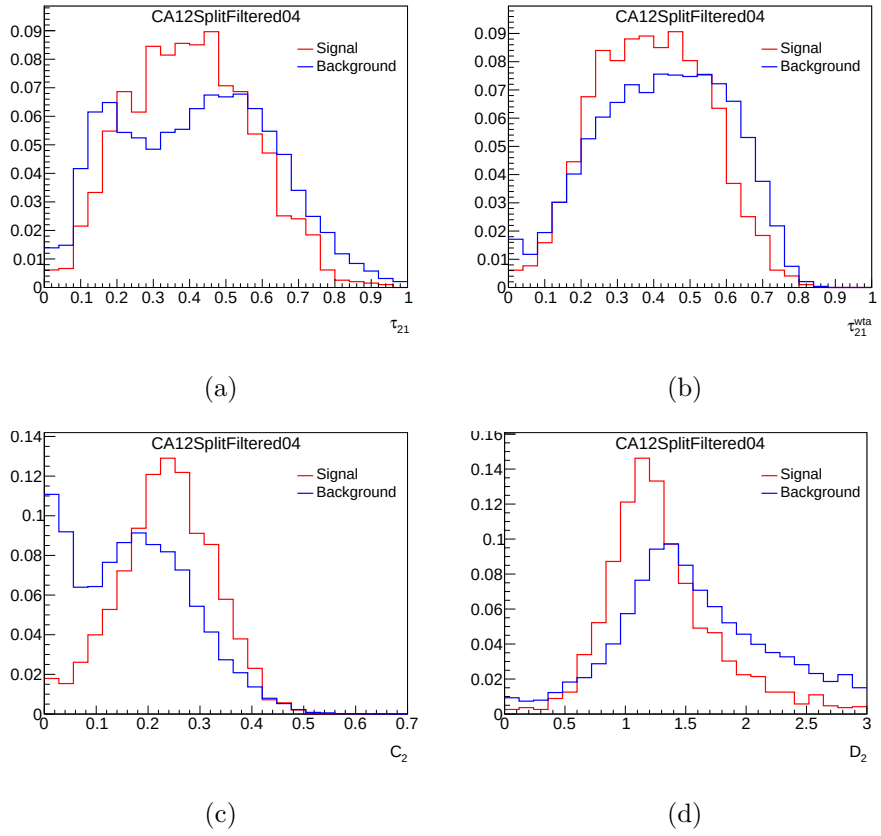

Figure B.3.: Substructure Distribution functions for the CA12SplitFiltered04 jet collection with $p_{\mathrm{T}} < 300\,\mathrm{GeV}$: (a) τ_{21}, (b) τ_{21}^{wta}, (c) C_2, (d) D_2.

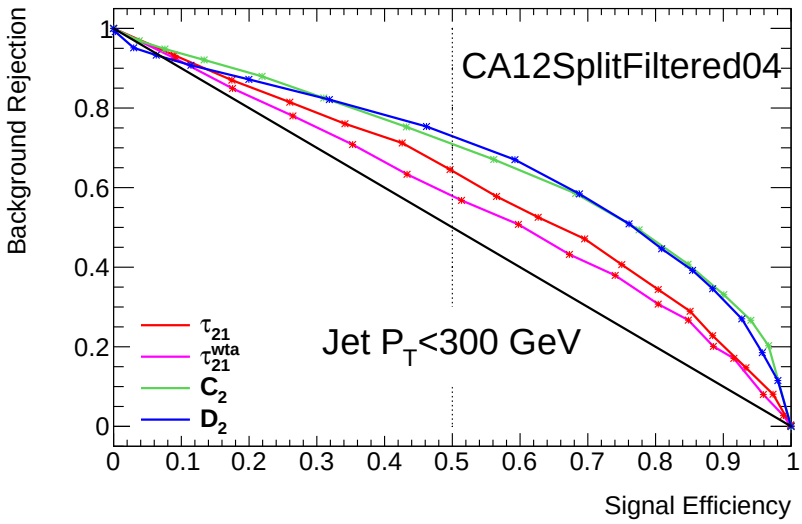

Figure B.4.: ROC curve showing the signal efficiency versus background rejection for the CA12SplitFiltered04 jet collection with $p_{\mathrm{T}} < 300\,\mathrm{GeV}$ for all substructure variables.

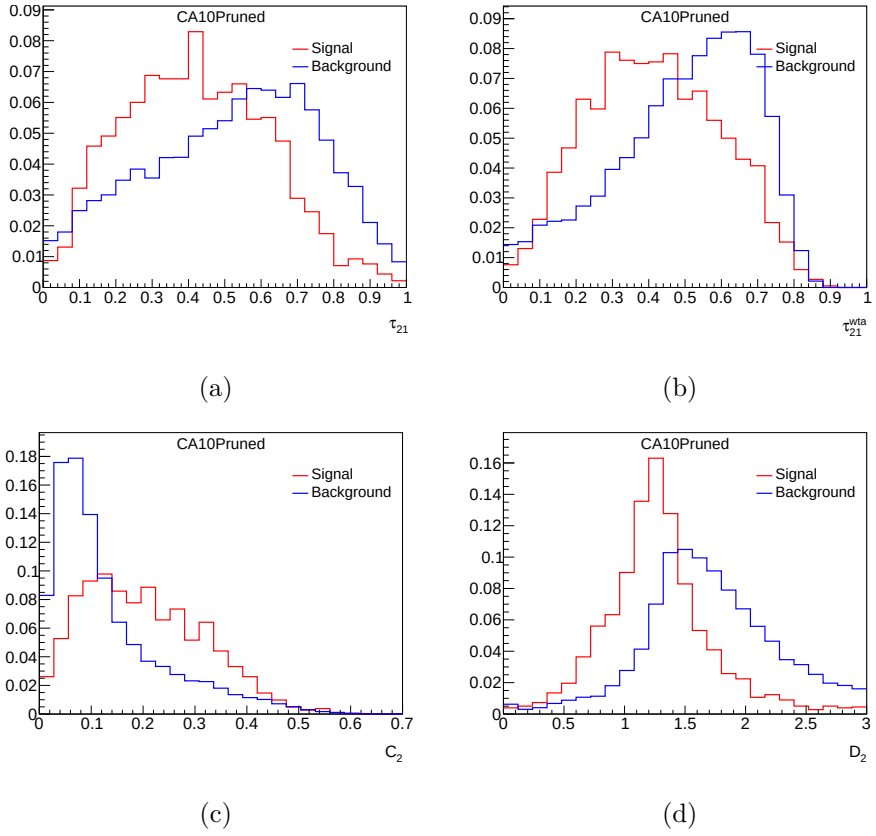

Figure B.5.: Substructure Distribution functions for the CA10Pruned jet collection with $p_T < 300\,\text{GeV}$: (a) τ_{21}, (b) τ_{21}^{wta}, (c) C_2, (d) D_2.

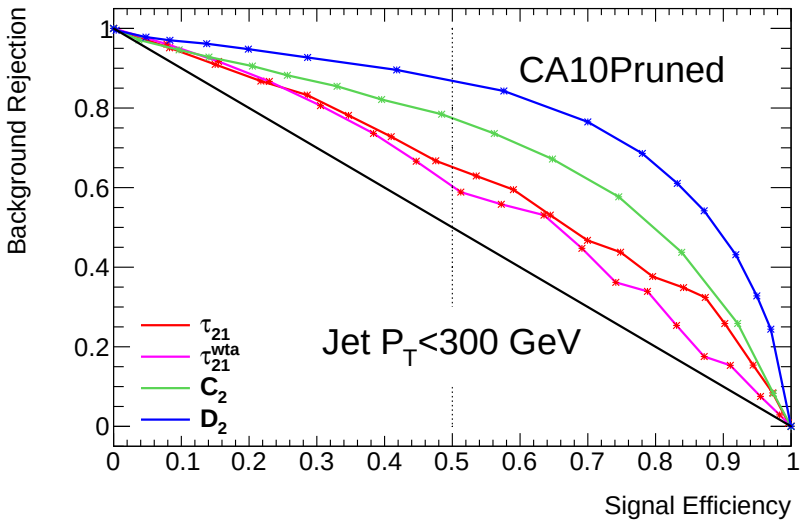

Figure B.6.: ROC curve showing the signal efficiency versus background rejection for the CA10Pruned jet collection with $p_T < 300\,\text{GeV}$ for all substructure variables.

C. ROC Curves and Substructure Distributions: Exclusive $p_T > 300\,\mathrm{GeV}$

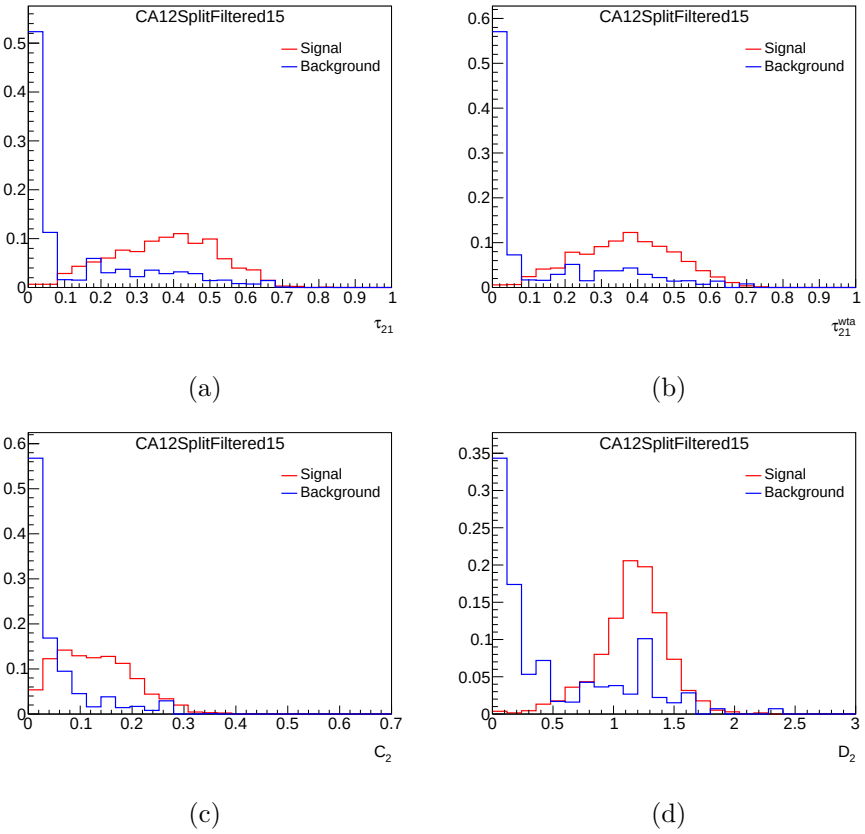

Figure C.1.: Substructure Distribution functions for the CA12SplitFiltered15 jet collection with $p_T \geq 300\,\text{GeV}$: (a) τ_{21}, (b) τ_{21}^{wta}, (c) C_2, (d) D_2.

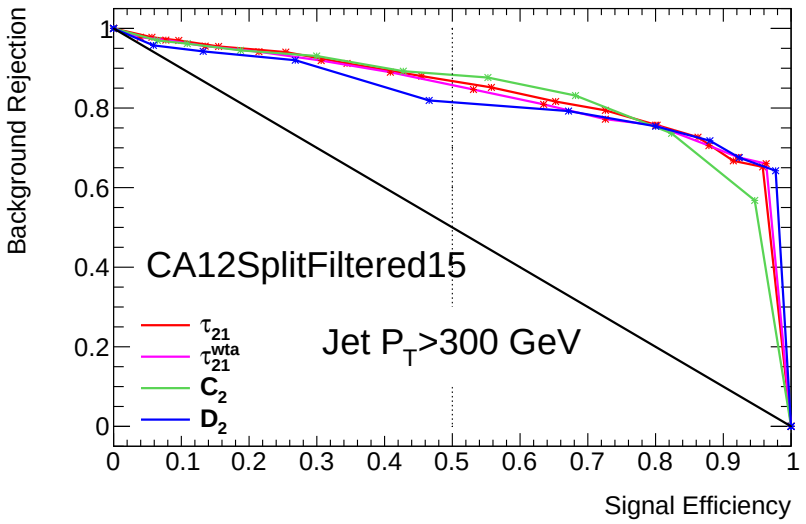

Figure C.2.: ROC curve showing the signal efficiency versus background rejection for the CA12SplitFiltered15 jet collection with $p_T \geq 300\,\text{GeV}$ for all substructure variables.

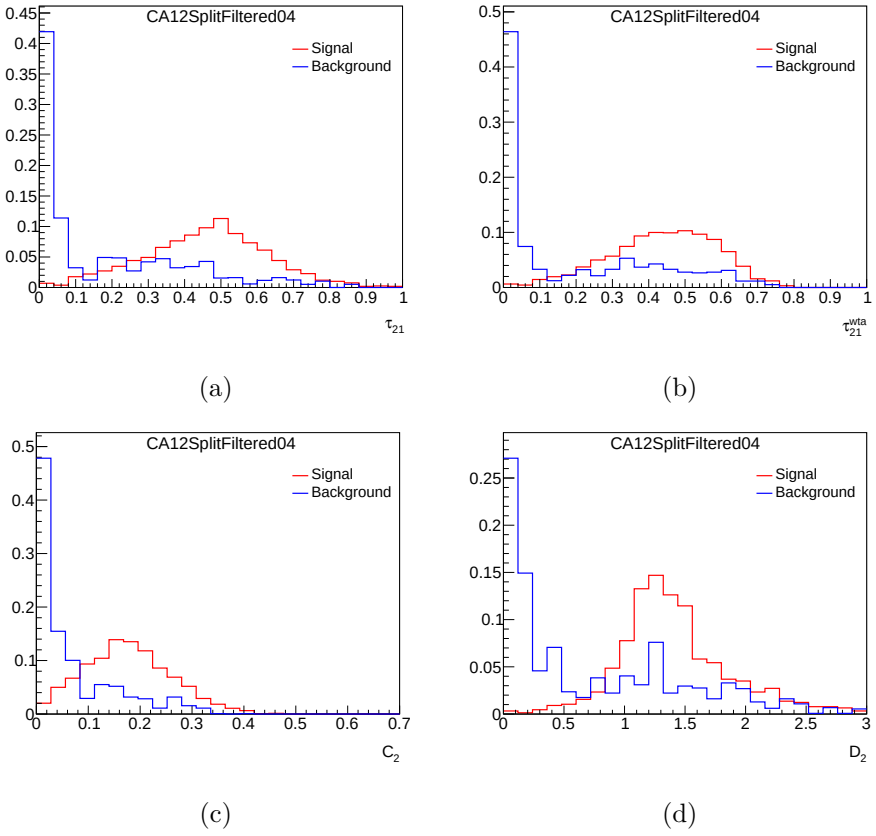

Figure C.3.: Substructure Distribution functions for the CA12SplitFiltered04 jet collection with $p_{\mathrm{T}} \geq 300\,\mathrm{GeV}$: (a) τ_{21}, (b) τ_{21}^{wta}, (c) C_2, (d) D_2.

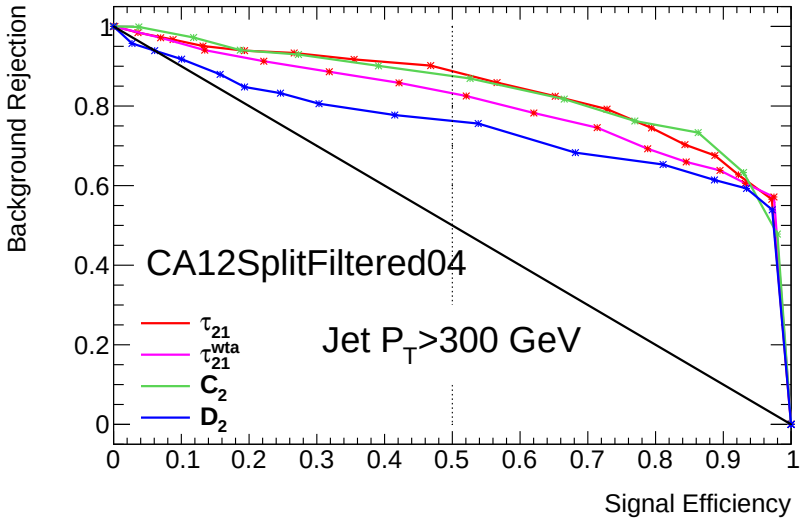

Figure C.4.: ROC curve showing the signal efficiency versus background rejection for the CA12SplitFiltered04 jet collection with $p_{\mathrm{T}} \geq 300\,\mathrm{GeV}$ for all substructure variables.

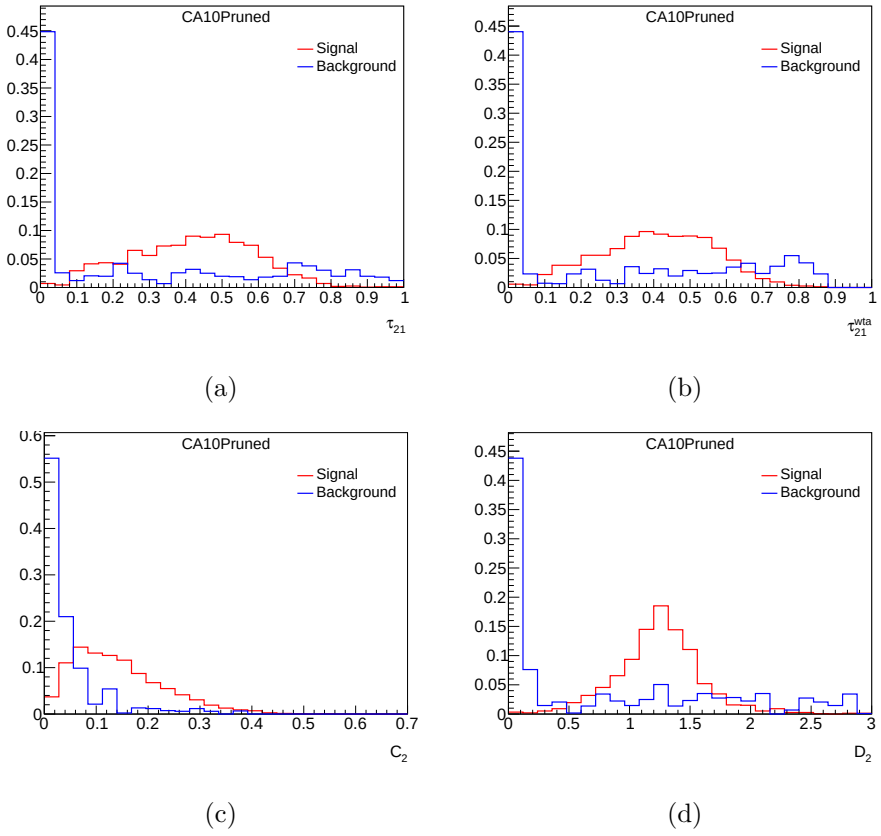

Figure C.5.: Substructure Distribution functions for the CA10Pruned jet collection with $p_T \geq 300\,\text{GeV}$: (a) τ_{21}, (b) τ_{21}^{wta}, (c) C_2, (d) D_2.

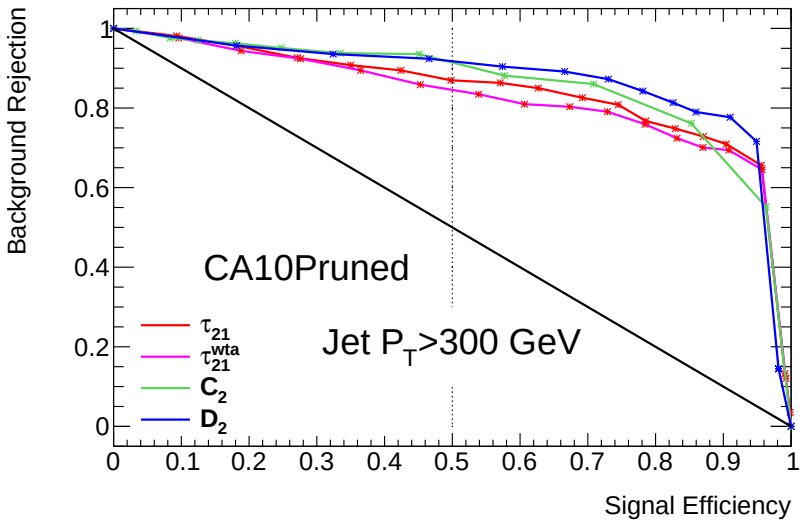

Figure C.6.: ROC curve showing the signal efficiency versus background rejection for the CA10Pruned jet collection with $p_T \geq 300\,\text{GeV}$ for all substructure variables.

Bibliography

[1] The ATLAS collaboration, *Observation of a new particle in the search for the Standard Model Higgs boson with the ATLAS detector at the LHC*, Phys. Lett. **B716**, 1 (2012)

[2] The CMS collaboration, *Observation of a new boson at a mass of 125 GeV with the CMS experiment at the LHC*, Phys. Lett. **B716**, 30 (2012)

[3] G. Branco, et al., *Theory and phenomenology of two-Higgs-doublet models*, Phys. Rept. **516**, 1 (2012)

[4] The ATLAS collaboration, *Search for pair production of Higgs bosons in the $b\bar{b}b\bar{b}$ final state using proton-proton collisions at $\sqrt{s} = 13$ TeV with the ATLAS detector* (2016)

[5] The ATLAS collaboration, *Search For Higgs Boson Pair Production in the $\gamma\gamma b\bar{b}$ Final State using pp Collision Data at $\sqrt{s} = 8$ TeV from the ATLAS Detector*, Phys. Rev. Lett. **114(8)**, 081802 (2015)

[6] X. Sun, H. Zhang, Y. Fang, *Search for Higgs pair production with decays to WW and $\gamma\gamma$ in 20.3 fb^{-1} proton-proton data at 8 TeV*, Technical Report ATL-COM-PHYS-2014-1446, CERN, Geneva (2014)

[7] M. Kobayashi, T. Maskawa, *CP Violation in the Renormalizable Theory of Weak Interaction*, Prog. Theor. Phys. **49**, 652 (1973)

[8] S. L. Glashow, *Partial Symmetries of Weak Interactions*, Nucl. Phys. **22**, 579 (1961)

[9] A. Salam, *Weak and Electromagnetic Interactions*, Conf. Proc. **C680519**, 367 (1968)

[10] S. Weinberg, *A Model of Leptons*, Phys. Rev. Lett. **19**, 1264 (1967)

[11] The ATLAS collaboration, The CMS collaboration, *Combined Measurement of the Higgs Boson Mass in pp Collisions at $\sqrt{s} = 7$ and 8 TeV with the ATLAS and CMS Experiments*, Phys. Rev. Lett. **114**, 191803 (2015)

[12] LHC Higgs Cross Section Working Group, *Handbook of LHC Higgs Cross Sections: 3. Higgs Properties: Report of the LHC Higgs Cross Section Working Group*, Technical Report arXiv:1307.1347. CERN-2013-004, Geneva (2013)

[13] G. D. Kribs, A. Martin, *Enhanced di-Higgs Production through Light Colored Scalars*, Phys. Rev. **D86**, 095023 (2012)

[14] R. Grober, M. Muhlleitner, *Composite Higgs Boson Pair Production at the LHC*, JHEP **06**, 020 (2011)

[15] S. Borowka, et al., *Higgs boson pair production in gluon fusion at NLO with full top-quark mass dependence*, Phys. Rev. Lett. **117(1)**, 012001 (2016)

[16] C.-Y. Chen, S. Dawson, I. M. Lewis, *Exploring resonant di-Higgs boson production in the Higgs singlet model*, Phys. Rev. **D91(3)**, 035015 (2015)

[17] T. Sjostrand, *A Model for Initial State Parton Showers*, Phys. Lett. **B157**, 321 (1985)

[18] B. R. Webber, *Fragmentation and hadronization*, Int. J. Mod. Phys. **A15S1**, 577 (2000)

[19] A. Buckley, et al., *General-purpose event generators for LHC physics*, Phys. Rept. **504**, 145 (2011)

[20] L. Evans, P. Bryant, *LHC Machine*, JINST **3**, S08001 (2008)

[21] The ATLAS collaboration, *ATLAS: Detector and physics performance technical design report. Volume 1* (1999)

[22] The ATLAS Collaboration, *The ATLAS Experiment at the CERN Large Hadron Collider*, Journal of Instrumentation **3(08)**, S08003 (2008)

[23] J. Alwall, et al., *The automated computation of tree-level and next-to-leading order differential cross sections, and their matching to parton shower simulations*, JHEP **07**, 079 (2014)

[24] J. Gao, et al., *CT10 next-to-next-to-leading order global analysis of QCD*, Phys. Rev. **D89(3)**, 033009 (2014)

[25] J. Bellm, et al., *Herwig 7.0/Herwig++ 3.0 release note*, Eur. Phys. J. **C76(4)**, 196 (2016)

[26] P. M. Nadolsky, et al., *Implications of CTEQ global analysis for collider observables*, Phys. Rev. **D78**, 013004 (2008)

[27] C. Oleari, *The POWHEG-BOX*, Nucl. Phys. Proc. Suppl. **205-206**, 36 (2010)

[28] T. Sjostrand, et al., *A Brief Introduction to PYTHIA 8.1*, Comput. Phys. Commun. **178**, 852 (2008)

[29] S. D. Ellis, D. E. Soper, *Successive combination jet algorithm for hadron collisions*, Phys. Rev. **D48**, 3160 (1993)

[30] The ATLAS Collaboration, *Performance of jet substructure techniques for large-R jets in proton-proton collisions at* $\sqrt{s}$ *= 7 TeV using the ATLAS detector*, JHEP **09**, 076 (2013)

[31] M. Cacciari, G. P. Salam, G. Soyez, *The Anti-k(t) jet clustering algorithm*, JHEP **04**, 063 (2008)

[32] Y. L. Dokshitzer, et al., *Better jet clustering algorithms*, JHEP **08**, 001 (1997)

[33] G. P. Salam, *Towards Jetography*, Eur. Phys. J. **C67**, 637 (2010)

[34] D. Krohn, J. Thaler, L.-T. Wang, *Jet Trimming*, JHEP **02**, 084 (2010)

[35] S. D. Ellis, C. K. Vermilion, J. R. Walsh, *Recombination Algorithms and Jet Substructure: Pruning as a Tool for Heavy Particle Searches*, Phys. Rev. **D81**, 094023 (2010)

[36] V. Khachatryan, et al. (CMS), *Identification techniques for highly boosted W bosons that decay into hadrons*, JHEP **12**, 017 (2014)

[37] J. M. Butterworth, et al., *Jet substructure as a new Higgs search channel at the LHC*, Phys. Rev. Lett. **100**, 242001 (2008)

[38] The ATLAS Collaboration, *Identification of boosted, hadronically decaying W bosons and comparisons with ATLAS data taken at* $\sqrt{s} = 8$ *TeV*, Eur. Phys. J. **C76(3)**, 154 (2016)

[39] J. Thaler, K. Van Tilburg, *Identifying Boosted Objects with N-subjettiness*, JHEP **03**, 015 (2011)

[40] A. J. Larkoski, D. Neill, J. Thaler, *Jet Shapes with the Broadening Axis*, JHEP **04**, 017 (2014)

[41] A. J. Larkoski, G. P. Salam, J. Thaler, *Energy Correlation Functions for Jet Substructure*, JHEP **06**, 108 (2013)

[42] A. J. Larkoski, I. Moult, D. Neill, *Power Counting to Better Jet Observables*, JHEP **12**, 009 (2014)

[43] Particle Data Group, *Review of Particle Physics**, Phys. Rev. D **86**, 010001 (2012)

Erklärung nach §13(9) der Prüfungsordnung für den Bachelor-Studiengang Physik und den Master-Studiengang Physik an der Universität Göttingen:

Hiermit erkläre ich, dass ich diese Abschlussarbeit selbständig verfasst habe, keine anderen als die angegebenen Quellen und Hilfsmittel benutzt habe und alle Stellen, die wörtlich oder sinngemäß aus veröffentlichten Schriften entnommen wurden, als solche kenntlich gemacht habe.
Darüberhinaus erkläre ich, dass diese Abschlussarbeit nicht, auch nicht auszugsweise, im Rahmen einer nichtbestandenen Prüfung an dieser oder einer anderen Hochschule eingereicht wurde.

Göttingen, den 30. September 2016

(Kieran Amos)